Graphical Abstract

Design of long-term stable concentrated colloidal dispersions in ionic liquids up to 473 K

J. C. Riedl,M. Sarkar,T. Fiuza,F. Cousin,J. Depeyrot,E. Dubois,G. Mériguet,R. Perzynski,V. Peyre

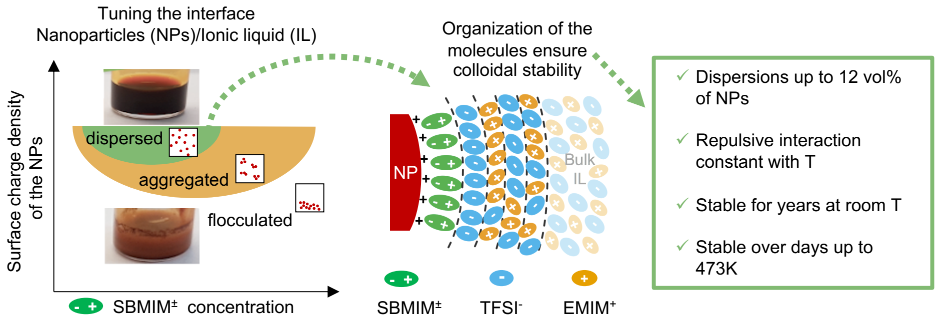

Design of long-term stable concentrated colloidal dispersions in ionic liquids up to 473 K

J. C. Riedl[a], M. Sarkar[a], T. Fiuza[a,b], F. Cousin[c], J. Depeyrot[b], E. Dubois[a,*], G. Mériguet[a], R. Perzynski[b] and V. Peyre[b,*]

[a]*Sorbonne Université, CNRS, Laboratoire PHENIX, 4 place Jussieu, case 51, 75005, Paris, France.*
[b]*Inst. de Fisica, Complex Fluid Group, Universidade de Brasília, Brasília, Brazil*
[c]*Laboratoire Léon Brillouin, UMR 12 CNRS-CEA, CEA-Saclay, 91191, Gif-sur-Yvette, France.*

ARTICLE INFO

Keywords:
Colloidal dispersions
Ionic liquids
Nanoparticles
Nanofluids
Ionanofluids

ABSTRACT

Hypothesis: Some of the most promising fields of application of ionic liquid-based colloids imply elevated temperatures. Their careful design and analysis is therefore essential. We assume that tuning the structure of the nanoparticle-ionic liquid interface through its composition can ensure colloidal stability for a wide temperature range, from room temperature up to 473 K.
Experiments: The system under study consists of iron oxide nanoparticles (NPs) dispersed in ethylmethylimidazolium bistriflimide (EMIM TFSI). The key parameters of the solid-liquid interface, tuned at room temperature, are the surface charge density and the nature of the counterions. The thermal stability of these nanoparticle dispersions is then analysed on the short and long term up to 473 K. A multiscale analysis is performed combining dynamic light scattering (DLS), small angle X-ray/neutron scattering (SAXS/SANS) and thermogravimetric analysis (TGA).
Findings: Following the proposed approach with a careful choice of the species at the solid-liquid interface, ionic liquid-based colloidal dispersions of iron oxide NPs in EMIM TFSI stable over years at room temperature can be obtained, also stable at least over days up to 473 K and NPs concentrations up to 12 vol% (≈30 wt%) thanks to few near-surface ionic layers.

---

1. Introduction

Ionic liquids (ILs) have a variety of properties such as high electrochemical and thermal stabilities, low vapour pressures, their abilities to dissolve many chemical species, and modest conductivities making them interesting for several fields of applications. Some examples are found in synthesis and catalysis processes [1], seals and bearings[2], as well as energy related applications [3, 4] such as batteries, supercapacitors and thermoelectric applications [5, 6, 7]. However, ionic liquids also have some properties hindering their industrial employment in some fields. For example they generally show elevated viscosities compared to molecular solvents which is connected to poor mass transport properties limiting the performance in energy applications at room temperature [3, 7]. However, the viscosity reduces significantly when the ionic liquids are heated up whereby this disadvantage (almost) vanishes [8]. Therefore, the use of ionic liquids at elevated temperatures is extremely interesting for applications. In addition, the performance of electrochemical devices is improved with increasing temperature. A way to further improve the system's properties at low and higher temperatures can be the addition of nanoparticles (NPs) to ionic liquids [9]. The addition of charged nanoparticles to electrolytes of electrochemical devices can, for instance, improve the thermoelectric properties compared with the solvent alone [10] or improve electrochemical performance compared with the pure IL [11]. Such dispersions of NPs can also be considered as potential heat transfer fluids thanks to their improved thermal properties [12, 13].

The colloidal stability of nanoparticle dispersions in ionic liquids can result from (i) polymers or molecules grafted on the NPs, (ii) molecules adsorbed on the NPs, (iii) the organization of the pure IL close to the NPs [9]. Among these options, the third one is privileged along with the addition of a small amount of species that can adsorb on the NPs. Indeed ion layering of the ionic liquid at the interface together with molecules that can absorb on the nanoparticle can produce a repulsive (oscillatory) forces that can outrank the attractive van der Waals forces between the nanoparticles and therefore colloidal stability is obtained [14, 15, 16, 17, 18, 19]. Such an ionic layering was shown by molecular dynamics (MD)

Abbreviations: ILs, Ionic liquids; NPs: nanoparticles; MD: molecular dynamics; σ, solid's surface charge density; $\Theta_{\mathrm{ion}}^{\mathrm{max}}$, maximum charge density of a densely packed counterion monolayer; EMIM TFSI, ethylmethylimidazolium bistriflimide; DLS, Dynamic Light Scattering; SAXS, Small Angle X-Ray Scattering; SANS, Small Angle Neutron Scattering; TEM, Transmission electron microscopy, TGA, thermogravimetric analysis; Φ_{NP}, nanoparticle's volume fraction; FAAS, flame atomic absorption spectroscopy; ESI-MS, electrospray ionization mass spectrometry; S(Q), structure factor; χ, osmotic compressibility; HTfO, triflic acid; HTFSI, N,N-Bis(trifluoromethanesulfonyl)imide acid; HSBMIM TFSI, 1-(4-Sulfobutyl)-3-methylimidazolium bistriflimide; HSBMIM TfO, 1-(4-Sulfobutyl)-3-methylimidazolium triflate; $SBMIM^{\pm}$, deprotonated form of $HSBMIM^{+}$, SFA, Surface Force Apparatus.

*Corresponding authors

✉ jesseriedl@web.de (J.C. Riedl); mitradeep.sarkar@gmail.com (M. Sarkar); thiagofiuza91@gmail.com (T. Fiuza); fabrice.cousin@cea.fr (F. Cousin); jerome.depeyrot@gmail.com (J. Depeyrot); emmanuelle.dubois@sorbonne-universite.fr (E. Dubois); guillaume.meriguet@sorbonne-universite.fr (G. Mériguet); regine.perzynski@sorbonne-universite.fr (R. Perzynski); veronique.peyre@sorbonne-universite.fr (V. Peyre)

ORCID(s): 0000-0001-9361-5132 (J.C. Riedl); 0000-0002-3431-0678 (M. Sarkar); 0000-0001-8859-0460 (T. Fiuza); 0000-0001-7523-5160 (F. Cousin); 0000-0002-1689-573X (J. Depeyrot); 0000-0001-8554-8486 (E. Dubois); 0000-0002-9921-0395 (G. Mériguet); 0000-0002-6634-6245 (R. Perzynski); 0000-0002-5129-1544 (V. Peyre)

simulations [14] and X-ray pair distribution analysis [15] of nanoparticle dispersions in molten salts [1] and some ionic liquids. However, this layered organization has been essentially studied on flat surfaces like sapphire, mica or gold for which many experiments like atomic force microscopy or X-Ray reflectivity are easier to perform [20, 21]. Elements of rationalization of the process have been brought by MD simulations of ionic liquids on flat surfaces, evidencing the crucial role of the ratio $\kappa_{\text{ion}} = |\sigma/\Theta_{\text{ion}}^{\text{max}}|$ with σ the solid's surface charge density and $\Theta_{\text{ion}}^{\text{max}}$ the maximum charge density of a densely packed counterion[2] monolayer [22]. For oxide NPs, σ can be tuned in a limited range changing the acidity of the medium or the nature of the surface. On the other hand, the counterions can be changed in the system, either by changing the ionic liquid itself or by adding ions.

Several works analysing ionic-liquid based colloids evidenced that these additional ions influence the colloidal stability despite their low concentration as compared to the ions concentration in the ionic liquid [17, 18, 23, 24, 25]. Furthermore, the nanostructure of the IL in contact with chargeable flat surfaces like graphite [26] or gold [27] is observed to be modified when adding extra small ions like Li^+ or Cl^-. These ions (even at low concentrations) have an influence as they can locate at the interface.

Besides, a long-range repulsion has been evidenced in ionic liquids and concentrated salt solutions [28, 29] by SFA force measurements between charged plates in various ILs. This repulsion, the mechanism of which is still under debate, extends over distances larger than the few layers formed close to the surface. Typically, the characteristic distance of this long-range repulsion is $\simeq 7$ nm at room temperature for EMIM TFSI between two symmetrical mica surfaces [29]. These forces, consistent with thermal disruption of electrostatic correlations and/or effective dissociation of ionic liquid ions, are closely related to the correlations induced in the presence of the charged surfaces in the bulk IL phase. However they are not well understood even in the most common conditions studied, at room temperature. Increasing temperature can have opposite effects on the different contributions, depending on their entropic or enthalpic nature [29]. Experimentally, the long range repulsion has been observed to depend on temperature and on IL nature, but in an equivocal manner: e.g. it decreases for mica surfaces in EMIM TFSI between 20 and 50 °C [30] whereas it increases or even appears for silica/mica surfaces in ethylammonium nitrate (EAN) between room temperature and 120 °C [31].

The use of ionic liquids at elevated temperatures is however extremely interesting for applications for example in the fields of heat transfer fluids [13], lubricants [32] or supercapacitors [11]. To be suitable, the ionic liquid-based systems need to be long-term stable at high temperature. This implies both chemical stability of the IL and colloidal stability of dispersions therein. Few studies have been performed above room temperature and fewer tried to analyze the nanostructure, both for ILs close to interfaces or for colloidal dispersions. Silica NPs dispersed in BMIM BF_4 were studied up to 60 °C, showing a change in interactions and rheological properties [33]. At higher temperature, only few nanoparticles in molten salts have been recently studied by Dynamic Light Scattering (DLS) on a range of temperature above their melting point [34].

Literature provides the decomposition temperature of the ILs in the short term, i.e. from classical thermogravimetric analysis (TGA) ramps, for a range of systems [35]. ILs based on fluorinated BF_4^-, $TFSI^-$ or TfO^- anions are among the most stable systems. After first measurements in several ILs based dispersions at high temperature[3], EMIM TFSI was chosen for a more focused study. This is indeed one of the most stable ILs, largely studied in literature because of its low viscosity [36].

In this work, the colloidal stability of NPs dispersions of (magnetic) iron oxides in EMIM TFSI is analyzed on the nanoscale taking care of the NP-IL interface. Always keeping the NPs in a liquid, NPs are transferred from water into pure IL or IL with additives, which allows us to control their initial surface charge and the nature of the associated counterions compensating this charge, thus tuning the ratio κ_{ion}. The dispersion state and the structure of the NPs on the nanoscale are first studied at room temperature, associating optical microscopy, dynamic light scattering (DLS) and small angle X-ray scattering (SAXS) measurements. In a second step, the optimal systems obtained are examined at high temperature up to 473 K (200 °C) combining DLS, SAXS, SANS as well as TGA. As the temperature at which the IL is stable in the long term (hours or months) can be up to a factor two lower than the short-term one from TGA ramps [35, 37], we performed isothermal TGA over hours and DLS measurements over days to determine suitability for applications.

2. Materials and Methods

2.1. Preparation of ionic liquid-based colloids

The products were purchased and used as received. They are listed in the ESI (S1). The same batch of maghemite (γ-Fe_2O_3) nanoparticles was used for all experiments. This batch was already used in reference [19], where the NPs' synthesis [38, 39] and the sample characteristics are described in detail. After a size sorting process, the fraction kept has a lognormal size distribution with a median diameter $d_{\text{NP}} = 8.7$ nm with a polydispersity index of $\sigma_d = 0.3$. At the end, the NPs are dispersed in water, their surface charge being positive, compensated by nitrate ions, with a pH of 1.8 and a volume fraction of 4.4 vol%.

To modify the charge and the counterions, sodium hydroxide is added to these dispersions at a volume fraction of 1 vol% till the point of zero charge is reached at pH≈7. The free ions are washed off several times with ultra-pure water. The

---

[1] analogue of ionic liquids with a melting temperature above 100°C

[2] ions of opposite charge compared to the surface

[3] Pyrr1(201)TFSI (1-Methyl-1-(2-Methoxyethyl) Pyrrolidinium TFSI), Pi1(201) TFSI (1-(2-Methoxyethyl)-1-Methyl Piperidinium TFSI), N1114 TFSI (N,N,N-triMethyl-N-Butyl Ammonium TFSI), N112(301) TFSI (N-Ethyl-N,N-diMethyl- N-(3-Methoxypropyl) Ammonium TFSI), EMIM FSI (EMIM bis(fluorosulfonyl)imide), EMIM TFO (EMIM trifluoromethanesulfonate).

particles can then be charged by protonation of the oxide surface with a strong acid. The charge density of the NPs σ increases while decreasing the pH and it is compensated by the conjugate anion of the acid. The pH is converted into a charge density according to the results obtained with similar NPs with nitric and perchloric acid [40], under the hypothesis that the surface charge does not depend on the nature of the strong acid used [40]. Concretely, pH values between 5 and 1.3 correspond to surface charge densities σ between 4 and 30 μC cm^{-2} (and the equivalent concentrations of added acids are between 0.0035 and 0.075 mol L^{-1}). This is the maximal reachable charge as lowering the pH too much can lead to the dissolution of the NPs.

Four strong acids are used here: N,N-Bis(trifluoromethanesulfonyl)imide acid (HTFSI), triflic acid (HTfO), 1-(4-Sulfobutyl)-3-methylimidazolium bistriflimide (HSBMIM TFSI), and 1-(4-Sulfobutyl)-3-methylimidazolium triflate (HSBMIM TfO), shown in Figure 1. $TFSI^-$ and TfO^- have different Θ^{max} values and the nature of the charged group differs. The 2 other acids HSBMIM TFSI and HSBMIM TfO are composed of two entities: the protonated cation $HSBMIM^+$ and the anion $TFSI^-$ or TfO^- [4]. The deprotonated form is thus composed of the zwitterion $SBMIM^\pm$ and the anion. The ratio between the two entities is one when adding them as one IL. However, this ratio can be varied by adding first HTFSI or HTfO and then $SBMIM^\pm$ (which is a powder). Doing so, the value of the charge density σ is varied independently of the amount of species of opposite charge. Figure 1 shows the 3 possible species that can play the role of counterions of the positive NPs.

Once the composition in water is fixed, an equivalent volume of the EMIM TFSI ionic liquid is added (see Figure 1) and the water is removed by freeze-drying. Therefore the final volume fraction Φ_{NP} in the ionic liquid is known (around 1 vol%) and the concentrations of the introduced species are also known.

When possible, more concentrated dispersions could be obtained by ultracentrifugation using an Optima 70 device and a type 100 Ti fixed-angle rotor from the company Beckman Coulter, USA. The samples need to be centrifuged at 55 000 rpm (243 000 g) for 24 hours at 19 °C. Separating the clear supernatant leads to concentrated samples with nanoparticle volume fractions $\Phi_{NP} \approx$ 10–20 vol% which can be diluted with their supernatant to appropriate intermediate concentrations.

2.2. Analyses of the samples

The ionic liquid-based colloids were analysed by transmission electron microscopy (TEM) using a JEOL-100 CX TEM in order to check that their transfer into the ionic liquid has not changed the shape of the nanoparticles compared to the initial sample in water, i.e there is no dissolution. A droplet of the ionic liquid-based ferrofluids (diluted to around 0.01 vol% with pure ionic liquid) was deposited on a carbon-coated copper grid and the back-side of the grid was swiped over a paper to remove as much liquid as possible.[5]

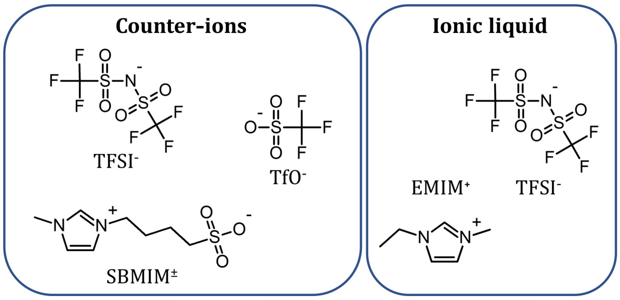

Figure 1: Structures of the ions 1-(4-butylsulfonate)-3-methylimidazolium ($SBMIM^\pm$), triflate (TfO^-), bis(trifluoromethylsulfonyl) amide ($TFSI^-$), and 1-ethyl-3-methylimidazolium ($EMIM^+$).

Then, on the micron scale, the existence of large agglomerates was checked by optical microscopy. If none were detected, the samples were analyzed by dynamic light scattering (DLS). Light scattering measurements were performed using Vasco, VascoFlex or VascoKin DLS Particle Analyzers from Cordouan Technologies to study translational diffusion properties of the ionic liquid-based colloids. Note that the viscosity of the ionic liquid-based colloids is difficult to know accurately as it depends on water traces [8] and on the other additives in the dispersions. However, performed together with other techniques, DLS can give complementary information and the properties of the samples can be analyzed in the long term over months. As measurements are performed at 1 vol% of NPs, only apparent hydrodynamic diameters d_H are given (see details in the ESI section S2).

Light scattering was coupled with small angle neutron scattering (SANS) up to 473 K (200 °C) for hours. The setup and the details of the experiments performed on the PAXY spectrometer at the LLB facility (CEA Saclay, France) are described in detail in the ESI section S3. Three different configurations were used leading to an accessible Q-range of 0.005 Å^{-1} to 0.2 Å^{-1}.

SAXS experiments were carried out with a laboratory instrument (XEUSS 2.0). The beam energy was fixed at 8 keV (λ = 1.54 Å). The sample to detector distance was 2.48 m to yield an accessible Q-range of 0.0045 Å^{-1}– 0.2 Å^{-1}. The samples absorb X-rays due to the ionic liquid EMIM TFSI and due to the iron atoms. Therefore thin capillaries were needed and the best compromise between absorption and scattered signal was obtained with 0.1 mm thick borosilicate capillaries from Vitrocom®. However, the wall thickness of 0.07 mm has an error of ±20 % and the interior thickness error is ±10 %. As a consequence, absolute intensity could hardly be determined and the high Q region ($>$ 0.1 Å^{-1}) was rather noisy. As a conclusion, the nanoparticle volume fraction together with the SANS measurements were used to adjust the SAXS curves to absolute intensities.

---

[4] Note that these two acids are ionic liquids when pure

[5] Note that TEM can not give a reliable insight on the dispersion state of NPs in solution because the preparation of the sample for the TEM measurements can affect the sample's nanostructure due to dilution and exposure to the humidity of the air.

The SAXS and SANS form factor $P(Q)$ of the nanoparticles were obtained from the extrapolation at 0 vol% of several dilute colloidal dispersions in water with low interparticle interactions. See the electronic supplementary information (ESI) of [19] for details and the corresponding curves. These form factors were used to determine structure factors $S(Q)$ from the measured intensity $I(Q)$ using:

$$S(Q) = \frac{I(Q)}{\Delta\rho^2 V_{\mathrm{NP}} \Phi_{\mathrm{NP}} P(Q)} \qquad (1)$$

where $\Delta\rho^2$ is the contrast and V_{NP} an average volume of the NP. The value of $S(Q \rightarrow 0)$ therefore compares the studied dispersions to a "reference" dispersion of individual nanoparticles without interparticle interaction. The difference can be due to interparticle interaction or to a change of the volume/form of the scattering objects (for example formation of small aggregates).

Isothermal and ramped temperature thermogravimetric analysis (TGA) were performed with a TGA 550 from TA Instruments. All samples (about 10–20 mg with the mass precision $\pm 0.1\ \mu$g) were measured in platinum pans and some samples were also measured in an alumina crucible. The nitrogen gas flow was 40 mL/min. Short-term temperature stabilities were conducted with a heating rate of 10 °C/min from room temperature up to 600 °C. Long-term temperature stabilities were measured at isothermal mode for several hours at the specified isothermal temperature with a heating rate of 20 °C/min from room temperature up to this temperature.

The nanoparticle volume fractions were deduced from the iron concentration determined by flame atomic absorption spectroscopy (FAAS) taking a density of 4.87 g cm^{-3}[41]. The technical details and the implementation of the techniques are detailed in the ESI of ref [19].

3. Results and discussion

3.1. Analysis of the dilute samples at 1 vol% at room temperature

Using the 4 strong acids to change the surface charge and SBMIM$^{\pm}$ to modify the surface, the σ–[SBMIM$^{\pm}$] plane, where σ is the initial surface charge density in water, can be explored to outline stability behaviors (see Figure 2). In these maps, the special case of the ratio SBMIM$^{\pm}$/ TFSI^{-} or TfO^{-} equal to one (easily reached when adding directly HSBMIM TFSI or HSBMIM TfO ILs) is shown with the brown line. Here, the quality of the dispersions in the IL is addressed with DLS measurements. These maps evidence that:

1) With TFSI^{-} or TfO^{-} counterions and [SBMIM$^{\pm}$] = 0, the NPs are floculated whatever the surface charge densities (from 4 to 30 μC cm^{-2}). This corresponds to the y-axis in Figure 2.

2) Adding SBMIM$^{\pm}$ to these systems can stabilize the nanoparticles if the surface charge density is high enough, which means that some SBMIM$^{\pm}$ localises at the solid liquid interface.

3) For a given amount of SBMIM$^{\pm}$ and for a given acid, the apparent hydrodynamic diameter d_{H} decreases while the surface charge density σ increases, when dispersions are obtained.

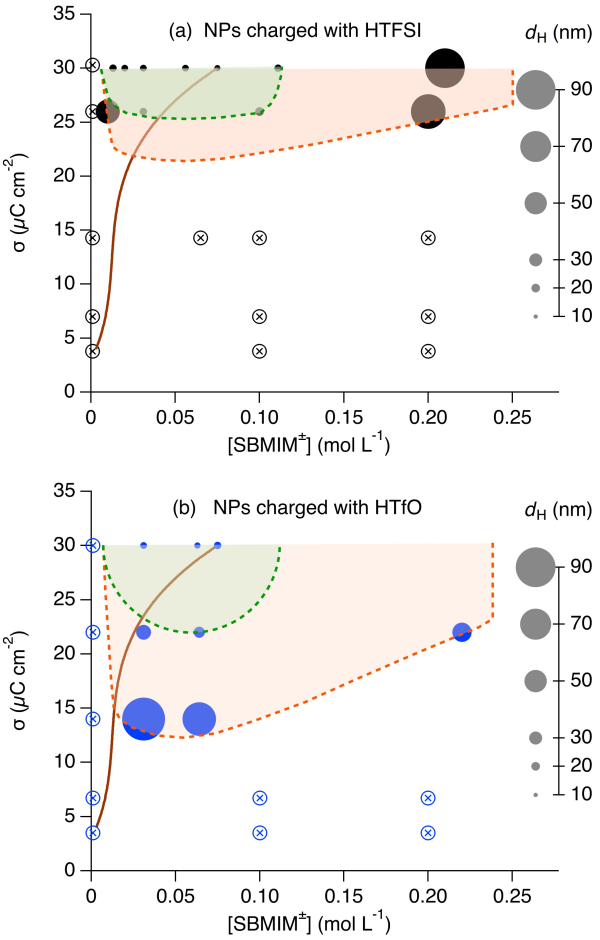

Figure 2: Maps of the nanostructure of the dispersions of nanoparticles in EMIM TFSI in the plane of the initial charge density of the NPs in water σ on the Y axis and of the added concentration of SBMIM$^{\pm}$ on the X axis. The symbols ⊗ correspond to aggregated samples. When DLS can be performed, the surface of the disks is proportional to the apparent size extracted from DLS (scale on the right). (a) σ increased by adding HTFSI; (b) σ increased by adding HTFO. The (calculated) brown line corresponds to [SBMIM$^{\pm}$]=[HTFSI] or [HTFO]. The green area indicates the region where the best samples are obtained. The red area indicates the region where samples are dispersed however with aggregates up to 90 nm.

4) For a given charge density σ, d_{H} depends on [SBMIM$^{\pm}$] and there is an optimal concentration for the minimal d_{H}. SAXS confirms that there is a change in the nanostructure while changing the concentration of SBMIM$^{\pm}$ for a given charge (see section S2 in ESI, Figure S1).

5) The final dispersion state in EMIM TFSI in the presence of SBMIM$^{\pm}$ depends on the initial counterion introduced, i.e. TFSI^{-} or TfO^{-}. For example for a surface charge density of 14 μC cm^{-2} (0.014 mol L^{-1} TfO^{-} or TFSI^{-} introduced with the added acid) and a SBMIM$^{\pm}$ concentration in the range 0.07–0.1 mol L^{-1} the apparent hydrodynamic diam-

eter for nanoparticle dispersions containing TfO^- is around 70 nm, although it is bigger than 100 nm for dispersions with $TFSI^-$.

The best dispersions states are obtained in the green areas of the maps (Figure 2). The optimal ones correspond to the maximal charge density $\sigma \approx 30\ \mu C\ cm^{-2}$. Among the intermediate $SBMIM^\pm$ concentrations in the green area, $[SBMIM^\pm] = 0.075$ mol L^{-1} appears to be the best of the tested values, as confirmed by SAXS (see section S2 in ESI). This corresponds to a ratio $SBMIM^\pm$ to $TFSI^-$ or $SBMIM^\pm$ to TfO^- of 1. It is thus easily reached by directly adding HSBMIM TFSI or HSBMIM TfO. SAXS also proves that several independent preparations with this composition are very reproducible (see section S2 in ESI, Figure S1).

3.2. The most stable samples: detailed nanostructure at room temperature, 1 vol%

The best dispersions obtained from the maps of Figure 2 are analyzed in details comparing the two systems (i) HSBMIM TFSI, where the anionic species are $TFSI^-$ and the sulfonate group of $SBMIM^\pm$; (ii) HSBMIM TfO, where the anionic species are $TFSI^-$, TfO^- and the sulfonate group of $SBMIM^\pm$ (the molecules are shown in Figure 1).

The images from transmission electron microscopy (TEM, Figure 3) show for both systems that the shape of the nanoparticles is not changed compared to the initial sample in water (TEM picture given in ref [19]). Moreover, the nanoparticles do not appear organized in the same way using HSBMIM TFSI or HSBMIM TfO: loose clusters are observed with HSBMIM TfO although the NPs seem more homogeneously dispersed with HSBMIM TFSI. However no definite conclusion can be extracted from the TEM images due to the perturbations induced by the measurement (see section 2.2).

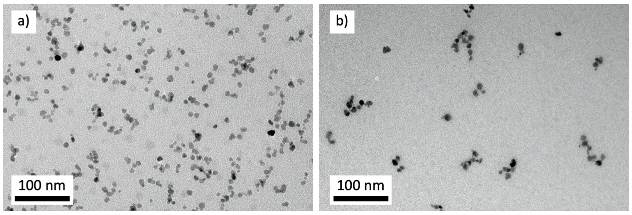

Figure 3: TEM images of nanoparticles dispersed in the ionic liquid EMIM TFSI with a) $[SBMIM^\pm] = 0.075$ mol L^{-1} and b) $[SBMIM^\pm] = [TfO^-] = 0.075$ mol L^{-1}. The ion structures are depicted in Figure 1. Both samples were diluted to a nanoparticle volume fraction $\Phi_{NP} \approx 0.01$ vol% with pure EMIM TFSI before the deposition of the ionic liquid-based colloid on the TEM grid.

Figure 4 plots the scattered intensity I(Q) by SAXS for these 2 samples and the reference form factor for comparison, at room temperature after the preparation and one year later. Figure 5 plots the structure factors S(Q) from SANS for these 2 samples (red curves). If $I(Q \rightarrow 0)/\Phi$ is larger than I(form factor), i.e. if $S(Q \rightarrow 0) > 1$, the interparticle interaction is attractive. If $I(Q \rightarrow 0)/\Phi$ is lower than I(form factor), i.e. if $S(Q \rightarrow 0) < 1$, the interparticle interaction is repulsive.

From both SAXS and SANS it can be deduced that the global interparticle interactions of the system with HSBMIM TfO is attractive ($S(Q \rightarrow 0) > 1$) and that of the system with HSBMIM TFSI is repulsive ($S(Q \rightarrow 0) < 1$). This shows that not only the zwitterion $SBMIM^\pm$ stabilises the nanoparticles but that introducing the additional anions TfO^-, although with a low concentration (0.075 mol L^{-1}) modifies the organisation of the molecules close to the NPs, and therefore the organisation of of the NPs. Moreover, both dispersions are stable in the long run as the scattering intensity after one year is similar to the initial one (Figure 4).

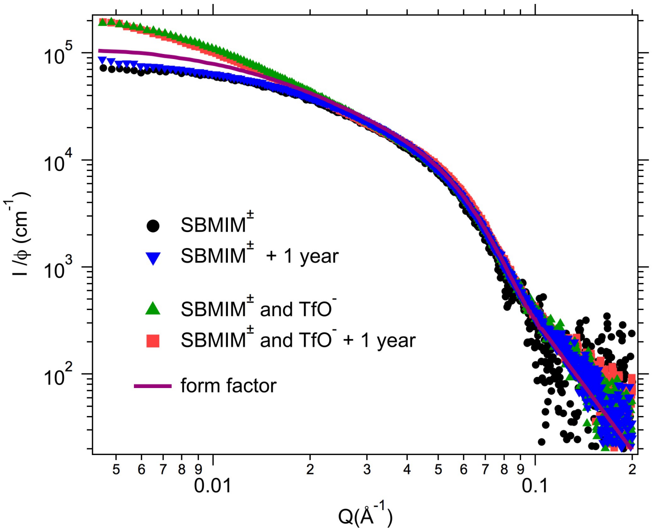

Figure 4: Absolute scattered intensities (normalized by the nanoparticle volume fraction $\Phi_{NP} \approx 1$ vol%) as a function of Q obtained by SAXS for dispersions of nanoparticles in EMIM TFSI one year apart Sample with $[SBMIM^\pm] = 0.075$ mol L^{-1} was stored in contact with (the moisture of) air. Sample with $[SBMIM^\pm] = [TfO^-] = 0.075$ mol L^{-1} was stored under dry atmosphere.

$S(Q \rightarrow 0)$ is related to the osmotic pressure Π by

$$S(Q \rightarrow 0) = \frac{kT}{V_{NP}} \frac{\partial \Phi_{NP}}{\partial \Pi} \qquad (2)$$

with V_{NP} the average volume of a nanoparticle. At a low volume fraction Φ_{NP}, the virial expansion of Π relates $S(Q \rightarrow 0)$ to the second order virial coefficient A_2 by:

$$S(Q \rightarrow 0) \simeq \frac{1}{1 + 2\ A_2 \Phi_{NP}} \qquad (3)$$

With measurements at one concentration only Φ_{NP}=1 vol%, and even with the required condition $2A_2\Phi_{NP} \ll 1$ not fulfilled, we tentatively give here an evaluation of A_2 (at least its sign is correct). We obtain here $A_2 \simeq -23$ for the attractive system and $A_2 \simeq 13$ for the repulsive one.

These results are consistent with the DLS measurements. For the repulsive dispersion with HSBMIM TFSI, d_H is approximately 12 nm (as for the initial water samples [19]), which proves that no aggregates are present. For the attractive dispersion with HSBMIM TfO, $d_H \approx 25$ nm, which

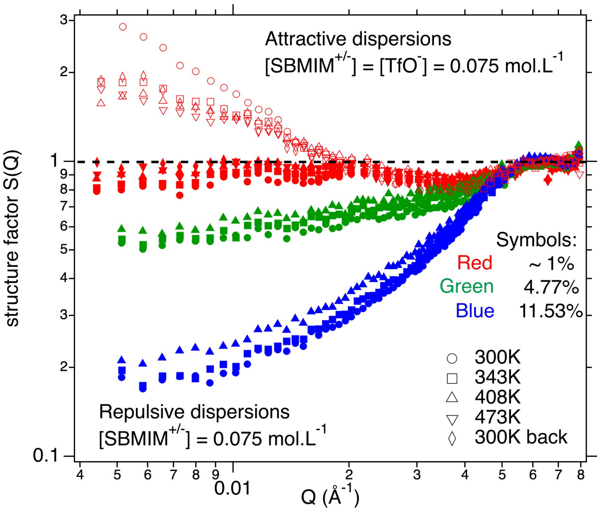

Figure 5: Structure factors $S(Q)$ obtained by small angle neutron scattering (SANS) as a function of the scattering vector Q for nanoparticle dispersions in EMIM TFSI. The symbols and colors are explained in the legends. Attractive dispersions with $[\mathrm{SBMIM}^{\pm}] = [\mathrm{TfO}^{-}] = 0.075$ mol L^{-1}, (empty red symbols): Note that the data at 27 °C before the heating cycle (empty red circles) are an experimental artifact, not observed with SAXS (see Figure 6). This is attributed to some pollution reversibly removed while heating. Repulsive dispersions with $[\mathrm{SBMIM}^{\pm}] = 0.075$ mol L^{-1} (full symbols): Note that there is no SANS at 200 °C for both concentrated samples due to leaks of the cells (SAXS and DLS with the remaining sample are used in Figure 6).

indicates the presence of small aggregates in the order of a few particles per aggregate.

3.3. Increasing the nanoparticles volume fraction at room temperature

Only the system made with HSBMIM TFSI could be largely concentrated as it is repulsive. Indeed, attractive ionic liquid-based colloids lead to a phase separation when increasing the volume fraction, as observed for citrated iron oxide NPs of similar size with various counterions in another IL [42].

The interparticle interactions are analyzed by SAXS and SANS measurements as a function of the nanoparticle volume fraction Φ_{NP}. The structure factors from SANS are plotted on Figure 5. The deduced values of $S(Q \to 0)$ by SAXS and SANS are shown in Figure 6. For a repulsive system, at a volume fraction Φ_{NP}, $S(Q \to 0)$ equals the osmotic compressibility $\chi(\Phi_{\mathrm{NP}})$, which decreases with increasing Φ_{NP}. In this case, the Carnahan-Starling expression for effective hard spheres [43, 44] can be used to analyze the compressibility χ up to large volume fractions as in references [24, 45, 46, 47, 48, 49, 50]. Equation (4) describes the compressibility

$$\chi(\Phi_{\mathrm{NP}}) = \chi_{\mathrm{CS}}(\Phi_{\mathrm{eff}}) = \frac{\left(1-\Phi_{\mathrm{eff}}\right)^4}{1+4\Phi_{\mathrm{eff}}+4\Phi_{\mathrm{eff}}^2-4\Phi_{\mathrm{eff}}^3+\Phi_{\mathrm{eff}}^4} \tag{4}$$

with

$$\Phi_{\mathrm{eff}} = \Phi_{\mathrm{NP}}\frac{d_{\mathrm{eff}}^3}{d_{\mathrm{NP}}^3} = \Phi_{\mathrm{NP}}\left(1+\frac{2\kappa^{-1}}{d_{\mathrm{NP}}}\right)^3 \tag{5}$$

and

$$d_{\mathrm{eff}} = d_{\mathrm{NP}} + 2\kappa^{-1} \tag{6}$$

In this model, an effective Hard Sphere, the radius of which is increased by a characteristic length κ^{-1}, accounts for the spatially decreasing interparticle interaction potential due to the ionic organization around the NPs (as the one produced by organized ions around NPs in polar solvents). The two-bodies interparticle interaction A_2 is then

$$A_2 = 4\frac{\Phi_{\mathrm{eff}}}{\Phi_{\mathrm{NP}}}. \tag{7}$$

The experimental data of the compressibility are fitted in Figure 6 with the Equations (4) and (5). The best fit is obtained for a fitting parameter $\kappa^{-1} \approx 1.0$ nm taking the average diameter $d_{\mathrm{NP}} = 8.7$ nm. This characteristic length is much smaller than the long-range interaction length frequently observed in IL by force measurements between charged surfaces [29]. It is related here to the organization of the ionic liquid layers localized close to the NPs. The extension of these layers is larger than κ^{-1}. Approximating the effective Hard Sphere potential by a decreasing exponential of characteristic length κ^{-1}, it would roughly extend up to 3-5 κ^{-1} hence over 3-5 nm. The two-bodies interparticle interaction A_2 is then $A_2 = 7.8 \pm 0.5$ which is almost the double of the hard sphere value $A_2^{\mathrm{HS}} = 4$ [43] and of the values obtained for citrate-coated oxide nanoparticles in ethylammonium nitrate with sodium counterions and smaller NPs ($A_2 = 4.6$) [18, 24].

3.4. Thermal stability of the most stable dispersions

The knowledge of the dispersions' behavior while heating is essential for the evaluation of the possible applications of such fluids. The two optimized systems are analyzed in details coupling several techniques on different scales: SANS and DLS up to 473 K (200 °C) and additional DLS and SAXS measurements before and after heating periods. Complementary TGA analyses are also presented, which brings an indirect and global information while heating.

3.4.1. Nanostructure

Given the limited allocated SANS beamtime, few temperatures were chosen (27 °C, 70 °C, 135 °C, 200 °C, and

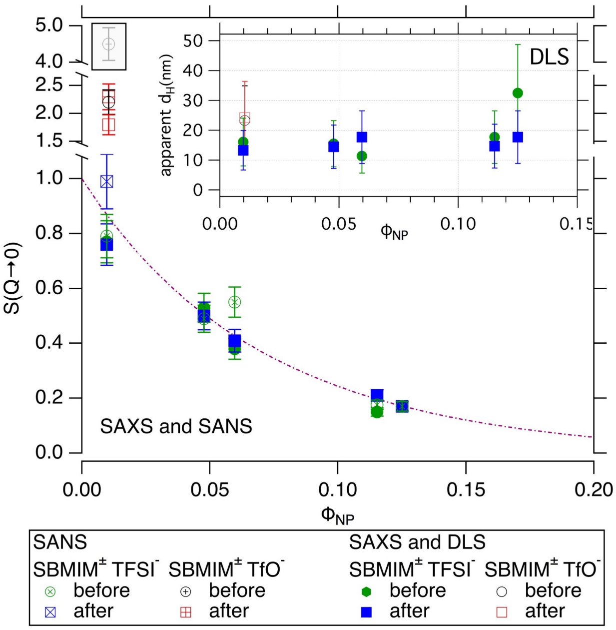

Figure 6: S(Q → 0) deduced from SAXS and SANS (data of Figure 5) measurements at room temperature for the repulsive system ([SBMIM±] = 0.075 mol L^{-1}) as a function of the nanoparticle volume fraction Φ_{NP} and for the attractive system ([SBMIM±] = [TfO⁻] = 0.075 mol L^{-1}) at Φ_{NP} = 1.04 vol%. The dashed-dotted line corresponds to the fit of the data for the repulsive samples with Equations (4) and (5) using $\Phi_{eff}/\Phi_{NP} = 1.82$ (two-bodies interparticle interaction quantified by the second virial coefficient $A_2 = 7.8 \pm 0.5$). **Inset**: apparent hydrodynamic diameter d_H as a function of the nanoparticle volume fraction Φ_{NP} for both systems. The data in the grey box is an artifact (see Figure 5). Both room temperature data before and after heating the samples for several hours up to 473 K (200 °C) are shown.

back at 27 °C) for the in-situ measurements of SANS and DLS up to 473 K (200 °C). For each step, DLS was performed after heating and enables checking that equilibrium is reached before measuring SANS. This is possible as the viscosity varies with temperature which influences the correlation function. Hence, stability of the correlation function means that viscosity and temperature are stable. DLS performed after SANS tells us whether some change occurred. One T step lasts around two hours, the whole cycle from 27 °C back to 27 °C around 10 hours. Such DLS data are presented in ESI, section S3, Figure S4. The SANS structure factors are plotted in Figure 5 and their extrapolation to $Q = 0$ in the inset. The structure factor at $Q = 0$ (from both SANS and SAXS) and the apparent d_H (from DLS) are plotted respectively in the main graph and the inset of Figure 6 before and after heating.

Looking first at the two samples at $\Phi_{NP} \approx 1$ vol% with different interfacial species, they show a weak evolution after they stay at high temperature. Indeed, the strong initial decrease of intensity for the attractive dispersions from 27 °C to 70 °C appears as an experimental artifact. The corresponding SAXS measurement at room temperature gives S(Q → 0) = 2.2 ± 0.2, which matches with the SANS after the cycle. Moreover, the DLS is similar before and after heating. This artifact can be due to some pollution (water, solvent,...) that is removed while heating. Leaving aside this point, the values of $S(Q \to 0)$ show that for this attractive sample, the same small aggregates/weak attractions remain whatever the temperature. Both the repulsive and the attractive sample appear stable on the time scale of the experiment. For the repulsive dispersions, the interaction remains repulsive whatever the temperature. However, given the small increase of $S(Q \to 0)$ at $\Phi_{NP} = 0.97$ vol% from 0.83 ± 0.08 to 0.98 ± 0.10 after heating, close to the error bar, a long-term experiment was performed. The sample was heated in a glass tube for several days at three temperatures up to 170 °C under vacuum and its state was checked with a DLS measurement at room temperature after each plateau. The results are summarized in Figure 7. The apparent hydrodynamic diameter is $d_H = 12 \pm 2$ nm showing that the sample is long-term stable at high temperature, here during 18 days.

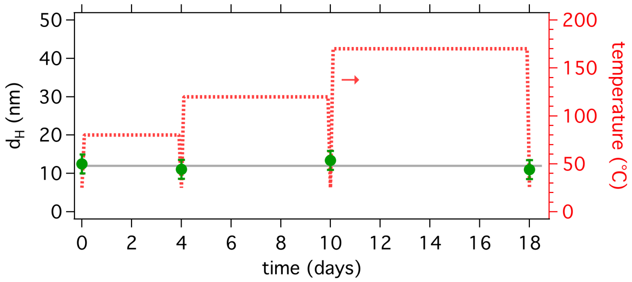

Figure 7: DLS measurements at room temperature for the repulsive dispersions at a nanoparticle volume fraction Φ_{NP} = 0.97 vol% shown in Figure 5 and 6. The sample was previously heated in a low vacuum around 10 mbar in an open bottle at the indicated temperatures for days. Note that the maximum temperature of the heating device is 170 °C. These DLS measurements at room temperature give extra information about temperature cycling.

The analysis of the concentrated repulsive samples by SANS, SAXS and DLS shows that the structure factors are close to those at room temperature and the compressibilities S(Q → 0) before and after heating are also quite similar (Figure 5 for SANS and Figure 6 for S(Q → 0)). The apparent d_H differ before and after heating for the concentrated samples (Figure 6, inset), with no systematic trend. We therefore attribute the variations to the difficulties of measurement of the concentrated samples in the furnace, which leads to large error bars.

All these elements converge towards the conclusion that the stability of these concentrated samples at high temperature is good, and that the same nanostructure and interaction are kept.

3.4.2. *Thermogravimetric analyses*

Such an analysis can be performed in different ways, the most classical being temperature heating ramps. However they correspond to short measurements and can overestimate the decomposition temperature. This is why other types of

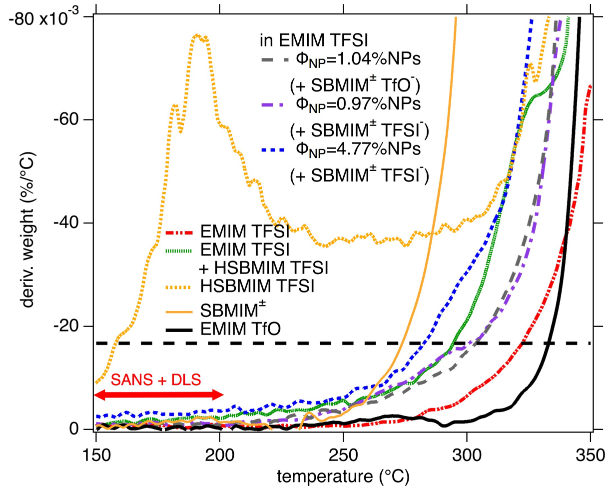

Figure 8: Ramped thermogravimetric analysis (TGA) measurements for the resulting dispersions in EMIM TFSI and for the components of these dispersions. Attractive and repulsive dispersions with $\Phi_{NP} \simeq 1$ vol%, repulsive dispersions with $\Phi_{NP} = 4.77$ vol%. EMIM TFSI and EMIM TfO without NPs are wet to mimic the worst amount of water that could remain in the dispersions. Dry SBMIM$^{\pm}$ and dry EMIM TFSI containing 2.5 wt% HSBMIM TFSI (amount present in the dispersions at 1 vol%) are also depicted. T_{start} (weight loss of 10 %/1h here) is indicated in the graph by the horizontal black dashed line. All the measurements are performed in Pt pans except HSBMIM TFSI for which an alumina crucible was used (see Figure S6 in ESI for more details).

measurements as isothermal ones over hours or longer times are also done here.

In a first step, heating ramps up to 873 K (600 °C) have been acquired for ILs without and with NPs. We will focus here on T_{start} (see caption of Figure 8), the temperature at which the sample starts to loose weight, which appears to be more relevant here than the most used T_{onset} (see ESI, section S3.2.). The raw data are shown in the ESI (Figure S5, section S3.2.), as well as the details on usual and used definitions, and the large table S1 gathers our values experimentally determined and values from literature. Note that T_{start} and long-term behaviors are scarce in literature, except for pure EMIM TFSI and EMIM TfO to a lesser extent. The derivative mass losses are plotted in Figure 8.

For the dispersions at $\Phi_{NP} \approx 1$ vol%, both attractive and repulsive, T_{start} equals 303 °C and is lowered by 20 °C for the repulsive sample at 4.77 vol%. This can be compared with the pure ILs, however the dispersions contain several species that should all be considered. T_{start} for the pure EMIM TFSI is 320 °C [35], a little higher than that for the 1 vol% dispersions. However, the IL may contain some water around the NPs. One or two water layers at the interface would correspond to 0.1–0.2 wt%. Therefore EMIM TFSI saturated with water at room temperature was measured, which corresponds to 0.5 wt%, a higher value nevertheless in the same range. Its T_{start} is close to the value from literature although T_{onset} is reduced by a few tens of degrees (ESI table S1). The other species are SBMIM$^{\pm}$, the zwitterion that is at the interface and possibly some HSBMIM. T_{start}(SBMIM$^{\pm}$) = 274 °C, which is still high. Pure HSBMIM TFSI appears to be the less stable species, that has to be measured in alumina crucibles as it seems to decompose in Pt pans close to room temperature (see Figure S6 in ESI, section S3.2.)[6]. T_{start}(HSBMIM TFSI) = 158 °C, which cannot be compared with literature as no data were found on this liquid. Only T_{onset} of IL of the same family (sulfoimidazolium) could be found [51, 52], showing values close to our results on HSBMIM TFSI (see table S1 in ESI). The last species, present in the attractive sample only, is TfO^{-} anions, the stability of which can be evaluated from EMIM TfO. Despite a high T_{onset} = 348 °C, the temperature at which 1% is lost after one year is 185°C, much lower than for EMIM TFSI (286°C) [53].

Finally, it appears important to mention that partial evaporation of the sample also leads to a weight loss although the sample is not decomposed. For example, EMIM TFSI is considered relatively volatile compared to other ionic liquids and its partial pressure at 200 °C is 0.02 Pa (calculated with the values of ref [53]), around a magnitude larger than for EMIM TfO. Note that the long-term stabilities after one year mentioned in the previous paragraph are corrected from the losses due to evaporation.

In a second step, isothermal TGA measurements at 200 °C during 15 h are performed on the repulsive samples to estimate their stability at this temperature (see Figure S7 of the ESI). The first analysis in classical Pt crucibles shows that the weight loss for the ionic liquid EMIM TfO is smaller than 0.1 % after 15 hours at 200 °C. For EMIM TFSI, the weight loss is a bit higher (0.2 %) and increases with the NPs volume fraction up to 1.5 vol%. The latter measurements reproduced in alumina crucible where the interference between HSBMIM and platinum is eliminated and the evaporation limited show a weight variation lower than 0.2 wt% after 15 hours for both the solvent and the dispersions, pointing towards a good stability of these repulsive dispersions at our maximal temperature of study of the nanostructure.

3.5. Discussion

Among the performed tests, four different types of interfaces are explored, each one in a specific range of NPs' charge and concentrations of the species that can localize at the interface. We discuss the differences of stability observed first at room temperature, then at temperature up to 473 K, i.e. 200 °C.

3.5.1. Room temperature

The four systems explore four different types of interfaces chosen to vary the ratio $\kappa_{ion}=|\sigma/\Theta^{max}_{ion}|$ where σ is the solid's surface charge density and Θ^{max}_{ion} the maximum charge density of a densely packed counterion monolayer [22]. It

---

[6] Note that using alumina crucibles for the other samples shifts the curves, which keep their shape (see Figure S6 in ESI). As these data are only used for comparisons of samples, only data with Pt pans are kept for all samples except HSBMIM TFSI.

was shown by MD simulations on flat surfaces of variable charge in the presence of one ionic liquid (one type of anion, one type of cation) that this ratio governs the organization close to the solid surface. A multilayered structure of positive and negative ions forms at the solid surface, the extention of which is maximal around $\kappa_{\text{ion}} \simeq 0.5$ [22, 54]. In the present systems, the initial density of charge σ in water can be varied through the acidity of the surrounding medium. Assuming a similar behaviour for the nanoparticle charge σ with the different counterions [40], σ is here tuned between 4 and 30 μC cm^{-2}. We assume that this charge is kept in the EMIM TFSI after transfer. $\Theta^{\text{max}}_{\text{ion}}$ is varied through the nature, thus the size, of the ions. Here the particles are positively charged, therefore the compensating ions are the anions. $|\Theta^{\text{max}}_{\text{TFSI}^-}| \approx 50\ \mu\text{C cm}^{-2}$ [55], $|\Theta^{\text{max}}_{\text{TfO}^-}| \approx 100\ \mu\text{C cm}^{-2}$ assuming that TfO^- is around half the size of the TFSI^- anion, and $|\Theta^{\text{max}}_{\text{SBMIM}^\pm}| \approx 35\mu\text{C cm}^{-2}$ considering that $\text{SBMIM}^\pm$ is a BMIM^+ cation with an extra sulfonate group leading to a slightly smaller $\Theta^{\text{max}}_{\text{ion}}$ value. By way of comparison, $|\Theta^{\text{max}}_{\text{EMIM}^+}| \approx 45\ \mu\text{C cm}^{-2}$.

In the first system, the positive NPs are in EMIM TFSI, and the TFSI^- anion is the only anionic species. Whatever the ratio κ_{ion} (from 0.08 to 0.6), a stable dispersion is never obtained. It means that the best ionic organization is not sufficient to counterbalance the attractive interactions.

In the second system, the positive NPs are still in EMIM TFSI however TfO^- anions are introduced while charging the NPs (adding HTfO). Their amount thus equals the number of charges of the NPs plus the amount associated with the free acid in the surrounding liquid. As sulfonate groups have a good affinity for the iron oxide surface [56], κ_{ion} is expected to be lower than for the first system, i.e. between 0.3 for an interface covered by TfO^- and 0.6 with no TfO^- present. It nevertheless does not lead to stable dispersions. Note that the same NPs in EMIM TfO, therefore with only TfO^- anions located at the NPs' interface ($\kappa_{\text{ion}} \simeq 0.3$), are also flocculated.

In the third system, a zwitterion is introduced, $\text{SBMIM}^\pm$. Its anionic group is a sulfonate, with a good affinity for iron oxide. Its cationic group is an imidazolium as the cationic group of the ionic liquid, EMIM TFSI. As summarized in the maps in Figures 2 and S1, there are thresholds of σ and $[\text{SBMIM}^\pm]$ above which dispersions exist, the quality of which varies a lot. The introduction of this zwitterion thus deeply modifies the interface, even at low concentrations and can lead to stable dispersions. The best dispersions (lower d_{H} and lower $S(0)$) are obtained for the highest charge density. However, NPs can be dispersed before a monolayer of $\text{SBMIM}^\pm$ covers the surface with a full layer of molecules perpendicular to the surface (around 0.02 mol L^{-1}). It means that either the zwitterions are tilted or that mixed layers with TFSI^- are formed. The analysis by SAXS shows that the lowest $S(0)$ (< 1, thus indicating the most repulsive interaction) are obtained for $\text{SBMIM}^\pm$ concentrations corresponding to values higher than a monolayer (within the hypothesis that all molecules are located at the interface). According to the estimation of $\Theta^{\text{max}}_{\text{ion}}$, a monolayer of $\text{SBMIM}^\pm$ at the maximal σ corresponds to κ_{ion} close to 1. Such a monolayer then shifts the positive charge of the NPs facing the IL by the length of the SBMIM molecule (8–10 Å) and adds a steric repulsive contribution to the interparticle interaction. The TFSI^- anions and the IL can then organize on top of $\text{SBMIM}^\pm$ layer. In this case, extent of the organization produces a sufficient repulsion and long-term stable (years) samples with a repulsive interparticle interaction that remain constant over time. Figure 9a shows a possible organization of the solid-liquid interface. Such an organization with few alternate layers of ions is several nanometers thick, which is compatible with the effective range determined from SANS/SAXS in section 3.3.

The fourth system is similar to the third one, however an amount of TfO^- anions equal to the number of $\text{SBMIM}^\pm$ zwitterions is introduced in the system. The trends are similar with σ and $\text{SBMIM}^\pm$, however this small TfO^- amount has dramatic effects: no repulsive systems are obtained with the explored parameters. There is always a weak attractive interaction, constant over time. This proves that the interface differs from the one in the third system. Now two sulfonate groups can compete at the iron oxide's interface: TfO^- and $\text{SBMIM}^\pm$, the former being much smaller then the latter. This will modify the first layer, which can no longer be considered as a simple shift of the NPs' surface, and as a consequence it will also modify the following layers. Figure 9b shows a possible organization of the solid-liquid interface.

3.5.2. High temperatures: macroscopic analysis up to 473 K

The next question is the behavior at high temperature of these stable dispersions obtained at room temperature. Both a microscopic (SANS, SAXS, DLS) and a macroscopic approach (TGA) have been used. The macroscopic approach by TGA raises the question of the criteria chosen and of the extrapolations to long-term behaviors. As already said before, T_{onset} and less frequently T_{start} are usually extracted from short-term measurements under gas flow. We choose the latter, as being more relevant for high T stability. On the long-term, several criteria have been defined: one example is a 1 % weight loss in 10 hours $T_{0.01/10\text{ h}}$ [35] and another one is the maximum temperature for an annual decomposition of 1 % $T_{\text{max},0.01/\text{year}}$ [57, 53], a value extrapolated from isothermal measurements on much shorter duration than 1 year. All these values are available here only for EMIM TFSI (see Table S1) and show that T_{start} and T_{onset} are much larger than $T_{0.01/10\text{ h}}$ or $T_{\text{max},0.01/\text{year}}$. Note that evaporation can occur and is usually not taken into account (except for $T_{\text{max},0.01/\text{year}}$ in table S1), so that the loss of mass measured is a mixture of evaporation and degradation, leading to a possible overestimation of degradation (see ESI section S3.2. for more details). Therefore at our maximal temperature of analysis for the ferrofluids here in SANS (200 °C), EMIM TFSI can be considered as long-term stable, with no degradation and only evaporation. Concerning the other compounds of the final dispersions, less information is available and only on

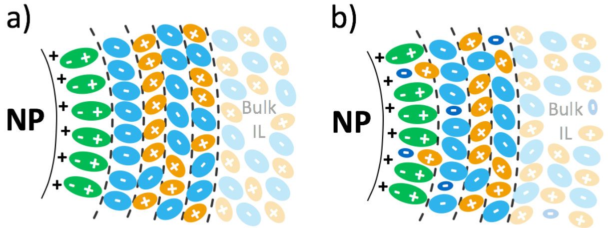

Figure 9: Schemes of possible organizations close to the NPs interface for the maximal surface charge density $\sigma \approx 30\ \mu\text{C cm}^{-2}$ and the most stable systems in EMIM TFSI. (a) repulsive system, the third in the discussion, with SBMIM± zwitterions at the interface, [SBMIM±] = 0.075 mol L^{-1}. (b) attractive systems, the fourth in the discussion, with SBMIM± zwitterions and TfO^- at the interface, [SBMIM±] = [TfO^-] = 0.075 mol L^{-1}.

pure compounds when it exists. EMIM TfO has been studied, however not HSBMIM TFSI. HSBMIM was tested in literature with HSO_4^- anions [51] and another sulfonate with a propyl group instead of a butyl, HSPMIM TfO, was also tested [52]. The average of their T_{onset} values are in the same range as our results on HSBMIM TFSI.

In ionic liquids, the possible mechanisms of degradation have been explored. Chen *et al.* [58] analyzed the temperature stability by TGA-MS of EMIM TFSI and found in their experiments that above 350 °C first TFSI decomposes to more nucleophilic groups, such as -F, $-CF_3$ and $-NH_2$ that mainly attack the ethyl group of the cation EMIM by elimination and nucleophilic substitution mechanisms. The same is observed for BMIM TfO that also decomposes to methylimidazolium (MIM) and HCF_3 [59]. Ethylimidazoles are the first species that are detected followed by methylimidazoles. SO_2 is also detected for $TFSI^-$ and as well for TfO^- based ionic liquids. Nakurte *et al* [60] analyzed by electrospray ionization mass spectrometry (ESI-MS) the decomposition mechanisms of different zwitterions dissolved in water, one being close to the zwitterion SBMIM± analyzed here but with a propyl instead of a butyl side chain. As observed in a lot of other studies for ionic liquids [37, 35, 58] it is the longer side chain of the imidazolium ring that is cleaved in the highest proportion (here 60 % in the mass spectrum) generating propanesulfonate and methylimidazolium. The second most probable mechanism is the elimination of sulfurous acid leaving methylpropyleneimidazolium (10 % in the mass spectrum).

From the literature, it appears that the thermal stability of ionic liquids is governed by nucleophilic anion attack of the cation. Thermal stability is therefore higher for lower nucleophilicity (i.e. higher Lewis basicity) [37]. As Lewis bases (for the anion) lower the degradation temperature, it is assumed that Lewis acids (for the cation) do as well. Hence, the (H)SBMIM could generate neutral molecules that evaporate.

From the measurements performed here on the components of the ferrofluids and on the ferrofluids, looking at T_{start} or T_{onset}, the colloidal dispersions appear chemically slightly less stable than pure EMIM TFSI (T_{start} shifted down by 20–40 °C) which seems to originate from HSBMIM. However the chemical stability is fully preserved at 200 °C on the scale of hours as shown by the long isothermal TGA experiments on 15 h at 200 °C.

3.5.3. *High temperatures: microscopic analysis up to 473 K*

The microscopic analysis of these same dispersions by SANS, SAXS and DLS complements this TGA analysis with the nanostructure at high temperature. The in-situ measurements at high temperature indicate that the interparticle interactions do not significantly evolve while increasing T up to 473 K. This is rather difficult to predict and even to interpret given the scarcity of studies at high temperatures. Indeed, the effect of temperature on colloidal stability can be examined from the point of view of interparticle forces [61]. In the systems studied here, particles are submitted to van der Waals and magnetic attractions. In order to prevent aggregation, some repulsion must counterbalance these forces. Among them, electrostatic interparticle interactions modeled with a Debye-Hückel expression is usually ruled out as totally screened because of the high concentration of ions [62]. Structural ionic interactions, stemming from the particular local organization of the IL solvent around the NPs in an ion layering close to the NPs' surface, correspond to a well-documented phenomenon at room temperature that indeed prevents close approach of the particles. H-bonds can also occur [33], but the high T stability of the system also rules them out here. A steric contribution, here due to the SBMIM± layer may also occur. However, the relatively short range of the interaction balance (characteristic length $\simeq$ 1 nm) observed by SANS and SAXS and its relative independence with temperature, is not compatible with the long-range repulsion, which has been frequently evidenced in ionic liquids and concentrated salt solutions by SFA force measurements [28, 29]. This long-range force of purely electrostatic origin typically extends for EMIM TFSI between symmetric mica surfaces, on a characteristic spacial length κ^{-1} of 6.6 nm at 22°C and decreases to 4.4 nm at 50°C [30], much larger than the value obtained here. The independence of the effective interparticle interaction on temperature obtained up to 473K here probably mainly result from the short range structuring forces of the ionic liquid. These forces are strongly dependent on the nature of the surface species and less dependent on T [30]. Moreover, a compensation between the variations of the different interactions can reduce this variation with temperature in the range 300-473 K.

4. Conclusions and outlook

The present study hypothesized that stable colloidal dispersions of nanoparticles (NPs) in ionic liquids (ILs) can be obtained by carefully adapting the NPs' interfacial properties with pure IL or adsorbed species and that they can be stable up to high temperatures, as high as 473 K (200 °C). Although such systems at high temperature are envisaged for heat transfer fluids [13] or lubricants [32], the charge of the

NPs is seldom considered and never varied. Moreover, the nanostructure of the dispersion at high temperature has only been considered recently by DLS in molten salts [34].

We show here how to change the dispersions state by playing on the NPs initial charge, which modulates the organization of the IL around the NPs in agreement with numerical simulations [15]. We also point at the role of the nature of the interfacial species and examine the role of the NPs volume fraction.

By associating transmission electron microscopy (TEM), dynamic light scattering (DLS), small angle scattering of X-rays (SAXS) or neutrons (SANS) for several compositions, we show that the pure IL alone does not provide colloidal stability to the dispersion. On the contrary, the zwitterion $SBMIM^{\pm}$ (a sulfonate imidazolium), which localizes at the NPs interface, can ensure stability at high NPs' charge density.

For the optimal amount of zwitterion at the maximal charge density of the NP, the colloidal stability is kept up to 473 K for Φ_{NP} from 1 to 12 vol%, with a global interparticle interaction that stays rather constant with temperature. It is quantified by a positive second virial coefficient of the osmotic pressure $A_2 \simeq 8$ associated with a rather short repulsion length $\kappa^{-1} \simeq 1$ nm. Unlike what is proposed in [29], small angle scattering measurements are unable here to detect the long range repulsion observed by SFA force measurements between symmetric charged surfaces in most ILs. It means anyway that the induced interfacial organization of the ions of the ionic liquid is sufficient to counterbalance the attractive van der Waals and magnetic dipolar interparticle interactions and that any modification induced while heating is compensated so that the colloidal dispersion remains stable.

We also show how additional species, such as TfO^- anions, can disturb the NPs-IL interface by localizing in this region and modify the NP-NP interaction, which becomes slightly attractive, with possible small aggregates. The obtained dispersions are nevertheless stable in the long run, over more than one year.

As the NPs are here magnetic, long-term stable ferrofluids are obtained stable over years at room temperature and at least on days at 473 K, suited for the use in applications that require a broad range of temperatures. The method can be extended to other ionic liquids and our tests show that stable dispersions can be obtained even above room temperature. In the future, it would be interesting to apply the principles to disperse NPs based on various oxides or other materials in ionic liquids, chosen for their respective properties, in order to design task specific dispersions.

Declaration of competing interest

There are no conflicts of interest to declare.

Authors contributions

JR did most experiments and wrote the first draft in the frame of his PhD, ED and VP supervised JR, added experiments and revised the text, JR,MS,TF,FC,ED,GM,RP,VP performed the scattering experiments. All the authors contributed to discussions and improvement of the text.

Acknowledgements

We thank Amandine Anfry for DLS measurements, Aude Michel for FAAS measurements, Arnaud Hélary for the design of the coupled DLS-SANS measurement setup at LLB (Laboratoire Léon Brillouin), and Sandra Casale for the TEM images taken at the IMPC (Institut des Matériaux de Paris-Centre). We acknowledge the Laboratoire Léon Brillouin (CEA-Saclay, France) for neutron beamtime at the PAXY spetrometer. This work has been supported by the European Union Horizon 2020 research and innovation program under the grant number 731976 (MAGENTA), by the Brazilian agency CNPq and the bilateral program CAPES-COFECUB Ph 950/20 and by the laboratories own resources.

Appendix A. Supplementary material

Electronic Supplementary Information (ESI) to this article can be found online at link.

References

[1] T. Welton, Room-Temperature Ionic Liquids. Solvents for Synthesis and Catalysis, Chemical Reviews 99 (8) (1999) 2071–2084. `doi:10.1021/cr980032t`.
URL `http://pubs.acs.org/doi/abs/10.1021/cr980032t`

[2] L. Mestrom, J. J. M. Lenders, R. de Groot, T. Hooghoudt, N. A. J. M. Sommerdijk, M. V. Artigas, Stable ferrofluids of magnetite nanoparticles in hydrophobic ionic liquids, Nanotechnology 26 (28) (2015) 285602. `doi:10.1088/0957-4484/26/28/285602`.
URL `http://stacks.iop.org/0957-4484/26/i=28/a=285602?key=crossref.39900d59c9edb1754ac24b6ebb3690ec`

[3] D. R. MacFarlane, N. Tachikawa, M. Forsyth, J. M. Pringle, P. C. Howlett, G. D. Elliott, J. H. Davis, M. Watanabe, P. Simon, C. A. Angell, Energy applications of ionic liquids, Energy Environ. Sci. 7 (1) (2014) 232–250. `doi:10.1039/C3EE42099J`.
URL `http://xlink.rsc.org/?DOI=C3EE42099J`

[4] M. Armand, F. Endres, D. R. MacFarlane, H. Ohno, B. Scrosati, Ionic-liquid materials for the electrochemical challenges of the future, in: Materials For Sustainable Energy: A Collection of Peer-Reviewed Research and Review Articles from Nature Publishing Group, World Scientific, 2011, pp. 129–137.

[5] M. Bonetti, S. Nakamae, B. T. Huang, T. J. Salez, C. Wiertel-Gasquet, M. Roger, Thermoelectric energy recovery at ionic-liquid/electrode interface, The Journal of Chemical Physics 142 (24) (2015) 244708. `arXiv:http://dx.doi.org/10.1063/1.4923199`, `doi:10.1063/1.4923199`.
URL `http://dx.doi.org/10.1063/1.4923199`

[6] E. Laux, S. Uhl, L. Jeandupeux, P. P. López, P. Sanglard, E. Vanoli, R. Marti, H. Keppner, Thermoelectric generators based on ionic liquids, Journal of Electronic Materials (2018) 1–5`doi:10.1007/s11664-018-6175-z`.
URL `https://doi.org/10.1007/s11664-018-6175-z`

[7] M. Dupont, D. MacFarlane, J. Pringle, Thermo-electrochemical cells for waste heat harvesting— progress and perspectives, Chem. Commun. 53 (2017) 6288–6302.

[8] K. Paduszyński, U. Domańska, Viscosity of Ionic Liquids: An Extensive Database and a New Group Contribution Model Based on a Feed-Forward Artificial Neural Network, Journal of Chemical Information

and Modeling 54 (5) (2014) 1311–1324. doi:10.1021/ci500206u.
URL http://pubs.acs.org/doi/10.1021/ci500206u

[9] Z. He, P. Alexandridis, Ionic liquid and nanoparticle hybrid systems: Emerging applications, Advances in Colloid and Interface Science 244 (2017) 54–70. doi:10.1016/j.cis.2016.08.004.
URL https://linkinghub.elsevier.com/retrieve/pii/S0001868616302238

[10] T. J. Salez, B. T. Huang, M. Rietjens, M. Bonetti, C. Wiertel-Gasquet, M. Roger, C. L. Filomeno, E. Dubois, R. Perzynski, S. Nakamae, Can charged colloidal particles increase the thermoelectric energy conversion efficiency?, Physical Chemistry Chemical Physics 19 (14) (2017) 9409–9416. doi:10.1039/C7CP01023K.
URL http://xlink.rsc.org/?DOI=C7CP01023K

[11] P. Bose, S. Bhattacharya, Electrochemical cycling behavior of pyrrolidinium ionic liquid tethered TiO2nanoparticle-hybrid electrolytes: Influence of grafting density, Journal of The Electrochemical Society 164 (12) (2017) H788–H797. doi:10.1149/2.1331712jes.
URL https://doi.org/10.1149/2.1331712jes

[12] J. M. P. França, M. J. V. Lourenço, S. M. S. Murshed, A. A. H. Pádua, C. A. Nieto de Castro, Thermal Conductivity of Ionic Liquids and IoNanofluids and Their Feasibility as Heat Transfer Fluids, Industrial & Engineering Chemistry Research 57 (18) (2018) 6516–6529. doi:10.1021/acs.iecr.7b04770.
URL https://pubs.acs.org/doi/10.1021/acs.iecr.7b04770

[13] A. A. Minea, S. M. Sohel Murshed, Ionic Liquids-Based Nanocolloids—A Review of Progress and Prospects in Convective Heat Transfer Applications, Nanomaterials 11 (4) (2021) 1039. doi:10.3390/nano11041039.
URL https://www.mdpi.com/2079-4991/11/4/1039

[14] H. Zhang, K. Dasbiswas, N. B. Ludwig, G. Han, B. Lee, S. Vaikuntanathan, D. V. Talapin, Stable colloids in molten inorganic salts, Nature 542 (7641) (2017) 328–331. doi:10.1038/nature21041.
URL http://www.nature.com/articles/nature21041

[15] V. Kamysbayev, V. Srivastava, N. B. Ludwig, O. J. Borkiewicz, H. Zhang, J. Ilavsky, B. Lee, K. W. Chapman, S. Vaikuntanathan, D. V. Talapin, Nanocrystals in Molten Salts and Ionic Liquids: Experimental Observation of Ionic Correlations Extending beyond the Debye Length, ACS Nano 13 (5) (2019) 5760–5770. doi:10.1021/acsnano.9b01292.
URL http://pubs.acs.org/doi/10.1021/acsnano.9b01292

[16] F. C. C. Oliveira, L. M. Rossi, R. F. Jardim, J. C. Rubim, Magnetic Fluids Based on γ-Fe$_2$O$_3$ and CoFe$_2$O$_4$ Nanoparticles Dispersed in Ionic Liquids, The Journal of Physical Chemistry C 113 (20) (2009) 8566–8572. doi:10.1021/jp810501m.
URL http://pubs.acs.org/doi/abs/10.1021/jp810501m

[17] M. Mamusa, J. Siriex-Plénet, F. Cousin, E. Dubois, V. Peyre, Tuning the colloidal stability in ionic liquids by controlling the nanoparticles/liquid interface, Soft Matter 10 (8) (2014) 1097. doi:10.1039/c3sm52733f.
URL http://xlink.rsc.org/?DOI=c3sm52733f

[18] M. Mamusa, J. Sirieix-Plénet, F. Cousin, R. Perzynski, E. Dubois, V. Peyre, Microstructure of colloidal dispersions in the ionic liquid ethylammonium nitrate: influence of the nature of the nanoparticles' counterion, Journal of Physics: Condensed Matter 26 (28) (2014) 284113. doi:10.1088/0953-8984/26/28/284113.
URL http://stacks.iop.org/0953-8984/26/i=28/a=284113?key=crossref.4f747615a635a1f7f3b19376218d5f56

[19] J. C. Riedl, M. A. Akhavan Kazemi, F. Cousin, E. Dubois, S. Fantini, S. Loïs, R. Perzynski, V. Peyre, Colloidal dispersions of oxide nanoparticles in ionic liquids: elucidating the key parameters, Nanoscale Advances 2 (4) (2020) 1560–1572, publisher: Royal Society of Chemistry. doi:10.1039/C9NA00564A.
URL https://pubs.rsc.org/en/content/articlelanding/2020/na/c9na00564a

[20] M. Mezger, H. Schroder, H. Reichert, S. Schramm, J. S. Okasinski, S. Schoder, V. Honkimaki, M. Deutsch, B. M. Ocko, J. Ralston, M. Rohwerder, M. Stratmann, H. Dosch, Molecular Layering of Fluorinated Ionic Liquids at a Charged Sapphire (0001) Surface, Science 322 (5900) (2008) 424–428. doi:10.1126/science.1164502.
URL http://www.sciencemag.org/cgi/doi/10.1126/science.1164502

[21] R. Hayes, N. Borisenko, M. K. Tam, P. C. Howlett, F. Endres, R. Atkin, Double layer structure of ionic liquids at the au(111) electrode interface: An atomic force microscopy investigation, J. Phys. Chem. C 115 (2011) 6855–6863.

[22] V. Ivaništšev, S. O'Connor, M. Fedorov, Poly(a)morphic portrait of the electrical double layer in ionic liquids, Electrochemistry Communications 48 (2014) 61–64. doi:10.1016/j.elecom.2014.08.014.
URL https://linkinghub.elsevier.com/retrieve/pii/S1388248114002690

[23] C. Guibert, V. Dupuis, J. Fresnais, V. Peyre, Controlling nanoparticles dispersion in ionic liquids by tuning the pH, Journal of Colloid and Interface Science 454 (2015) 105–111. doi:10.1016/j.jcis.2015.04.059.
URL https://linkinghub.elsevier.com/retrieve/pii/S0021979715004361

[24] K. Bhattacharya, M. Sarkar, T. J. Salez, S. Nakamae, G. Demouchy, F. Cousin, E. Dubois, L. Michot, R. Perzynski, V. Peyre, Structural, Thermodiffusive and Thermoelectric Properties of Maghemite Nanoparticles Dispersed in Ethylammonium Nitrate, ChemEngineering 4 (1) (2020) 5, number: 1 Publisher: Multidisciplinary Digital Publishing Institute. doi:10.3390/chemengineering4010005.
URL https://www.mdpi.com/2305-7084/4/1/5

[25] J. Nordström, L. Aguilera, A. Matic, Effect of Lithium Salt on the Stability of Dispersions of Fumed Silica in the Ionic Liquid BMImBF $_4$, Langmuir 28 (9) (2012) 4080–4085. doi:10.1021/la204555g.
URL http://pubs.acs.org/doi/10.1021/la204555g

[26] A. Elbourne, S. McDonald, K. Voïchovsky, F. Endres, G. G. Warr, R. Atkin, Nanostructure of the Ionic Liquid–Graphite Stern Layer, ACS Nano 9 (7) (2015) 7608–7620. doi:10.1021/acsnano.5b02921.
URL http://pubs.acs.org/doi/10.1021/acsnano.5b02921

[27] R. Hayes, N. Borisenko, B. Corr, G. B. Webber, F. Endres, R. Atkin, Effect of dissolved LiCl on the ionic liquid–Au(111) electrical double layer structure, Chemical Communications 48 (82) (2012) 10246. doi:10.1039/c2cc35737b.
URL http://xlink.rsc.org/?DOI=c2cc35737b

[28] J. Zeman, S. Kondrat, C. Holm, Bulk ionic screening lengths from extremely large-scale molecular dynamics simulations, Chem. Commun. 56 (2020) 15635–15638. doi:10.1039/D0CC05023G.
URL http://dx.doi.org/10.1039/D0CC05023G

[29] M. A. Gebbie, A. M. Smith, H. A. Dobbs, A. A. Lee, G. G. Warr, X. Banquy, M. Valtiner, M. W. Rutland, J. N. Israelachvili, S. Perkin, R. Atkin, Long range electrostatic forces in ionic liquids, Chemical Communications 53 (7) (2017) 1214–1224. doi:10.1039/C6CC08820A.
URL http://xlink.rsc.org/?DOI=C6CC08820A

[30] M. A. Gebbie, H. A. Dobbs, M. Valtiner, J. N. Israelachvili, Long-range electrostatic screening in ionic liquids, Proc Natl Acad Sci USA 112 (24) (2015) 7432–7437. doi:10.1073/pnas.1508366112.
URL http://www.pnas.org/lookup/doi/10.1073/pnas.1508366112

[31] N. Hjalmarsson, R. Atkin, M. W. Rutland, Switchable long-range double layer force observed in a protic ionic liquid, Chemical Communications 53 (3) (2017) 647–650, number: 3. doi:10.1039/C6CC07396D.
URL http://xlink.rsc.org/?DOI=C6CC07396D

[32] X. Shi, W. Huang, X. Wang, Ionic liquids-based magnetic nanofluids as lubricants, Lubrication Science 30 (2) (2018) 73–82. doi:10.1002/ls.1405.
URL http://doi.wiley.com/10.1002/ls.1405

[33] J. Gao, P. M. Mwasame, N. J. Wagner, Thermal rheology and microstructure of shear thickening suspensions of silica nanoparticles dispersed in the ionic liquid [C $_4$ mim][BF $_4$], Journal of Rheology 61 (3) (2017) 525–535. doi:10.1122/1.4979685.
URL http://sor.scitation.org/doi/10.1122/1.4979685

[34] N. Navarrete, A. Gimeno-Furió, J. Forner-Escrig, J. E. Juliá, R. Mondragón, Colloidal stability of molten salt –based nanofluids: Dynamic Light Scattering tests at high temperature conditions, Powder Technology 352 (2019) 1–10. doi:10.1016/j.powtec.2019.04.045.
URL https://linkinghub.elsevier.com/retrieve/pii/

S0032591019302931

[35] Y. Cao, T. Mu, Comprehensive Investigation on the Thermal Stability of 66 Ionic Liquids by Thermogravimetric Analysis, Ind. Eng. Chem. Res. 53 (20) (2014) 8651–8664. doi:10.1021/ie5009597.
URL https://pubs.acs.org/doi/10.1021/ie5009597

[36] S. Werner, M. Haumann, P. Wasserscheid, Ionic Liquids in Chemical Engineering, in: Prausnitz, JM and Doherty, MF and Segalman, RA (Ed.), Annual Review of Chemical and Biomolecular Engineering, Vol 1, Vol. 1 of Annual Review of Chemical and Biomolecular Engineering, Annual Reviews, 2010, pp. 203–230. doi:10.1146/annurev-chembioeng-073009-100915.

[37] C. Maton, N. D. Vos, C. V. Stevens, Ionic liquid thermal stabilities: decomposition mechanisms and analysis tools, Chemical Society Reviews 42 (13) (2013) 5963–5977. doi:10.1039/C3CS60071H.
URL https://pubs.rsc.org/en/content/articlelanding/2013/cs/c3cs60071h

[38] R. Massart, Preparation of aqueous magnetic liquids in alkaline and acidic media, IEEE transactions on magnetics 17 (2) (1981) 1247–1248.

[39] J.-P. Jolivet, E. Tronc, Interfacial electron transfer in colloidal spinel iron oxide. Conversion of Fe_3o_4-γ-Fe_2o_3 in aqueous medium, Journal of Colloid and Interface Science 125 (2) (1988) 688–701. doi:10.1016/0021-9797(88)90036-7.
URL http://linkinghub.elsevier.com/retrieve/pii/0021979788900367

[40] I. T. Lucas, S. Durand-Vidal, E. Dubois, J. Chevalet, P. Turq, Surface Charge Density of Maghemite Nanoparticles: Role of Electrostatics in the Proton Exchange, J. Phys. Chem. C 111 (50) (2007) 18568–18576. doi:10.1021/jp0743119.
URL https://pubs.acs.org/doi/10.1021/jp0743119

[41] U. Schwertmann, R. M. Cornell, Iron Oxides in the Laboratory: Preparation and Characterization, John Wiley & Sons, 2008, google-Books-ID: yfOrDwOvCYkC.

[42] M. Mamusa, J. Sirieix-Plénet, R. Perzynski, F. Cousin, E. Dubois, V. Peyre, Concentrated assemblies of magnetic nanoparticles in ionic liquids, Faraday Discussions 181 (2015) 193–209. doi:10.1039/C5FD00019J.
URL http://xlink.rsc.org/?DOI=C5FD00019J

[43] N. F. Carnahan, K. E. Starling, Thermodynamic Properties of a Rigid-Sphere Fluid, The Journal of Chemical Physics 53 (2) (1970) 600–603. doi:10.1063/1.1674033.
URL http://aip.scitation.org/doi/10.1063/1.1674033

[44] J. A. Barker, D. Henderson, Perturbation Theory and Equation of State for Fluids. II. A Successful Theory of Liquids, The Journal of Chemical Physics 47 (11) (1967) 4714–4721. doi:10.1063/1.1701689.
URL http://aip.scitation.org/doi/10.1063/1.1701689

[45] M. Sarkar, J. C. Riedl, G. Demouchy, F. Gélébart, G. Mériguet, V. Peyre, E. Dubois, R. Perzynski, Inversion of thermodiffusive properties of ionic colloidal dispersions in water-DMSO mixtures probed by forced Rayleigh scattering, Eur. Phys. J. E 42 (6) (2019) 72. doi:10.1140/epje/i2019-11835-6.
URL https://doi.org/10.1140/epje/i2019-11835-6

[46] M. Kouyaté, C. L. Filomeno, G. Demouchy, G. Mériguet, S. Nakamae, V. Peyre, M. Roger, A. Cēbers, J. Depeyrot, E. Dubois, R. Perzynski, Thermodiffusion of citrate-coated γ-Fe $_2o_3$ nanoparticles in aqueous dispersions with tuned counter-ions – anisotropy of the Soret coefficient under a magnetic field, Physical Chemistry Chemical Physics 21 (2019) 1895–1903. doi:10.1039/C8CP06858E.

[47] E. Wandersman, A. Cēbers, E. Dubois, G. Mériguet, A. Robert, R. Perzynski, The cage elasticity and under-field structure of concentrated magnetic colloids probed by small angle X-ray scattering, Soft Matter 9 (48) (2013) 11480. doi:10.1039/c3sm51961a.
URL http://xlink.rsc.org/?DOI=c3sm51961a

[48] C. L. Filomeno, M. Kouyaté, V. Peyre, G. Demouchy, A. F. C. Campos, R. Perzynski, F. A. Tourinho, E. Dubois, Tuning the Solid/Liquid Interface in Ionic Colloidal Dispersions: Influence on Their Structure and Thermodiffusive Properties, The Journal of Physical Chemistry C 121 (10) (2017) 5539–5550. doi:10.1021/acs.jpcc.6b10280.
URL http://pubs.acs.org/doi/10.1021/acs.jpcc.6b10280

[49] C. Lopes Filomeno, M. Kouyaté, F. Cousin, G. Demouchy, E. Dubois, L. Michot, G. Mériguet, R. Perzynski, V. Peyre, J. Sirieix-Plénet, F. Tourinho, Ionic magnetic fluids in polar solvents with tuned counter-ions, Journal of Magnetism and Magnetic Materials 431 (2017) 2–7. doi:10.1016/j.jmmm.2016.07.050.
URL https://linkinghub.elsevier.com/retrieve/pii/S0304885316315633

[50] R. Cabreira Gomes, A. Ferreira da Silva, M. Kouyaté, G. Demouchy, G. Mériguet, R. Aquino, E. Dubois, S. Nakamae, M. Roger, J. Depeyrot, R. Perzynski, Thermodiffusion of repulsive charged nanoparticles – the interplay between single-particle and thermoelectric contributions, Phys. Chem. Chem. Phys. 20 (24) (2018) 16402–16413. doi:10.1039/C8CP02558D.
URL http://xlink.rsc.org/?DOI=C8CP02558D

[51] J. Gui, H. Ban, X. Cong, X. Zhang, Z. Hu, Z. Sun, Selective alkylation of phenol with tert-butyl alcohol catalyzed by Brönsted acidic imidazolium salts, Journal of Molecular Catalysis A: Chemical 225 (1) (2005) 27–31. doi:10.1016/j.molcata.2004.08.026.
URL https://linkinghub.elsevier.com/retrieve/pii/S1381116904006077

[52] A. S. Amarasekara, O. S. Owereh, Thermal properties of sulfonic acid group functionalized Brönsted acidic ionic liquids, J Therm Anal Calorim 103 (3) (2011) 1027–1030. doi:10.1007/s10973-010-1101-5.
URL http://link.springer.com/10.1007/s10973-010-1101-5

[53] F. Heym, B. J. M. Etzold, C. Kern, A. Jess, Analysis of evaporation and thermal decomposition of ionic liquids by thermogravimetrical analysis at ambient pressure and high vacuum, Green Chem. 13 (6) (2011) 1453. doi:10.1039/c0gc00876a.
URL http://xlink.rsc.org/?DOI=c0gc00876a

[54] V. Ivanistsev, M. V. Fedorov, Interfaces between Charged Surfaces and Ionic Liquids: Insights from Molecular Simulations, Interface magazine 23 (1) (2014) 65–69. doi:10.1149/2.F08141if.
URL https://iopscience.iop.org/article/10.1149/2.F08141if

[55] S. A. Kislenko, Y. O. Moroz, K. Karu, V. B. Ivaništšev, M. V. Fedorov, Calculating the Maximum Density of the Surface Packing of Ions in Ionic Liquids, Russian Journal of Physical Chemistry A 92 (5) (2018) 999–1005. doi:10.1134/S0036024418050187.
URL http://link.springer.com/10.1134/S0036024418050187

[56] X. Lu, S. Deng, B. Wang, J. Huang, Y. Wang, G. Yu, Adsorption behavior and mechanism of perfluorooctane sulfonate on nanosized inorganic oxides, Journal of Colloid and Interface Science 474 (2016) 199–205. doi:10.1016/j.jcis.2016.04.032.
URL https://linkinghub.elsevier.com/retrieve/pii/S0021979716302521

[57] A. Seeberger, A.-K. Andresen, A. Jess, Prediction of long-term stability of ionic liquids at elevated temperatures by means of non-isothermal thermogravimetrical analysis, Phys. Chem. Chem. Phys. 11 (41) (2009) 9375. doi:10.1039/b909624h.
URL http://xlink.rsc.org/?DOI=b909624h

[58] Y. Chen, Y. Cao, Y. Shi, Z. Xue, T. Mu, Quantitative Research on the Vaporization and Decomposition of [EMIM][Tf $_2$ N] by Thermogravimetric Analysis–Mass Spectrometry, Ind. Eng. Chem. Res. 51 (21) (2012) 7418–7427. doi:10.1021/ie300247v.
URL https://pubs.acs.org/doi/10.1021/ie300247v

[59] H. Ohtani, S. Ishimura, M. Kumai, Thermal Decomposition Behaviors of Imidazolium-type Ionic Liquids Studied by Pyrolysis-Gas Chromatography, Anal. Sci. 24 (10) (2008) 1335–1340. doi:10.2116/analsci.24.1335.
URL http://joi.jlc.jst.go.jp/JST.JSTAGE/analsci/24.1335?from=CrossRef

[60] I. Nakurte, P. Mekss, K. Klavins, A. Zicmanis, G. Vavilina, S. Dubrovina, Collision-Induced Dissociation of Imidazolium-Based Zwitterionic Liquids, Eur J Mass Spectrom (Chichester) 15 (4) (2009) 471–478. doi:10.1255/ejms.997.
URL http://journals.sagepub.com/doi/10.1255/ejms.997

[61] Z. He, P. Alexandridis, Nanoparticles in ionic liquids: interactions and organization, Physical Chemistry Chemical Physics 17 (28)

(2015) 18238–18261. doi:10.1039/C5CP01620G.
URL http://xlink.rsc.org/?DOI=C5CP01620G

[62] R. Kjellander, Nonlocal electrostatics in ionic liquids: The key to an understanding of the screening decay length and screened interactions, The Journal of Chemical Physics 145 (12) (2016) 124503. arXiv:https://doi.org/10.1063/1.4962756, doi:10.1063/1.4962756.
URL https://doi.org/10.1063/1.4962756

Design of long-term stable concentrated colloidal dispersions in ionic liquids up to 473 K

J. C. Riedl[1], M. Sarkar[1], T. Fiuza[1,2], F. Cousin[3], J. Depeyrot[2], E. Dubois[1,*], G. Mériguet[1], R. Perzynski[1], and V. Peyre[1,*]

[1]Sorbonne Université, Laboratoire PHENIX, 4 place Jussieu, case 51, 75005, Paris, France
[2]Inst. de Fisica, Complex Fluid Group, Universidade de Brasília, Brasília, Brazil
[3]Laboratoire Léon Brillouin, UMR CNRS 12, CE Saclay, Gif sur Yvette, France
[*]emmanuelle.dubois@sorbonne-universite.fr, veronique.peyre@sorbonne-universite.fr

SUPPLEMENTARY INFORMATION

S1 Materials

The following materials were used without further purification: Sodium hydroxide (NaOH pellets, 98 %, Acros Organics); hydrochloric acid (HCl, 37 % water solution, AnalaR Normapur); iron(II) chloride ($FeCl_2$*$4H_2O$, AnalaR Normapur, VWR); iron(III) chloride ($FeCl_3$*$6H_2O$, Prolabo); iron(III) nitrate ($Fe(NO_3)_3$*$9H_2O$, technical, VWR); triflic acid (HTfO, 49.2 wt% in water, purity 99 %, SOLVIONIC); N,N-Bis(trifluoromethanesulfonyl)imide acid (HTFSI, purity 95 %, Fluorochem); 1-(4-Sulfobutyl)-3-methylimidazolium bistriflimide (HSBMIM TFSI, purity 98 %, SOLVIONIC); 1-(4-Sulfobutyl)-3-methylimidazolium triflate (HSBMIM TfO, purity 98 %, SOLVIONIC); 1-(4-Sulfobutyl)-3-methylimidazolium ($SBMIM^{\pm}$, purity 98 %, SOLVIONIC).

S2 Colloidal stabilities at $\Phi_{NP} \simeq 1$ vol%

This section presents additional results about the colloidal stability. Firstly, Figure S1 presents SAXS results for some samples presented in Figure 2 of the main text, and this SAXS supports the DLS results. Indeed, the doubt in DLS results from the uncertainty on the viscosity of the medium in the present case. An apparent hydrodynamic diameter is extracted, using the Stokes-Einstein relation:

$$D = \frac{k_B T}{3\pi\eta d_H} \tag{1}$$

with the Boltzmann constant k_B, the absolute temperature T, and the solvent shear-viscosity η. In the calculation of the apparent hydrodynamic diameter d_H (apparent because the interparticle interaction is forgotten in this equation) only the viscosity of EMIM TFSI is considered. However in the studied dispersions, HTFSI is introduced first to tune the NPs' charge, then $SBMIM^{\pm}$ is added to vary the ratio between $TFSI^-$ and $SBMIM^{\pm}$ (two step process). Part of the $SBMIM^{\pm}$ moves to the NPs interface, and the other part can either stay in the IL or can catch an H^+ to form HSBMIM. In this latter case, the dispersing medium becomes a mixture of EMIM TFSI and HSBMIM TFSI, this latter ionic liquid having a very high viscosity (≈1700 cP at 25 °C). It would thus change the viscosity of the dispersing medium by a factor up to 2 for the maximal amount of HSBMIM TFSI in the solvent if we assume a linear influence of its weight fraction on the viscosity. Hence, the apparent hydrodynamic diameter plotted could be overestimated by a factor of up to 2. SAXS enables to separate the existence of aggregates from hidden viscosity effects. Figure S1 shows that the $S(Q \rightarrow 0)$ values reproduce the same trend as d_H however less pronounced. This confirms that it is mainly the nanostructure that changes, however, together with an additional influence of the viscosity with increasing $SBMIM^{\pm}$ concentration.

Secondly, Figure S1 shows that several sample preparations with the same composition are perfectly reproducible, the SAXS curves being superimposed. This was done on samples at the maximal charge in water with the "one step process" adding the HSBMIM TFSI ionic liquid directly, which also improves reproducibility.

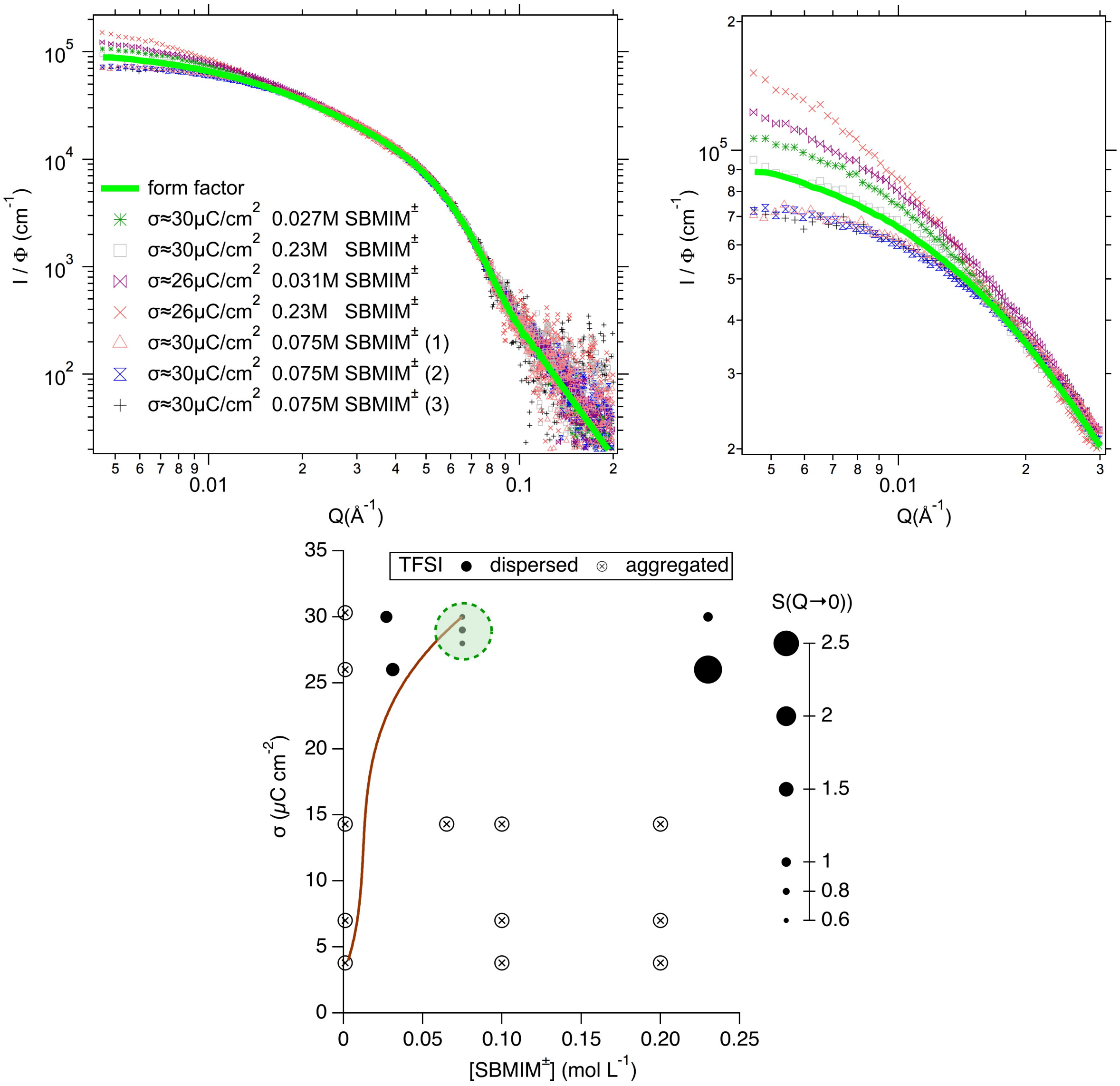

Figure S1. Top) Absolute scattered intensities (normalized by the nanoparticle volume fraction $\Phi_{NP} \approx 0.8$-1 vol%) as a function of Q obtained by SAXS for nanoparticle dispersions in EMIM TFSI as a function of [SBMIM$^{\pm}$] (same principle as the maps of Figure 2 in the main text). σ is the initial charge density of the NPs in water. The samples are prepared with the two step process (acid first, then SBMIM$^{\pm}$ zwitterion) except the last three, marked (1), (2), and (3). They are prepared with the one step process in the same way to test the reproducibility (see text for details). The figure on the right is a zoom of the small Q region that clearly shows the difference between the samples as well as the good reproducibility for several independent preparations; Bottom) The corresponding S(Q→0) values for the samples which are not aggregated in the plane σ/[SBMIM$^{\pm}$]. The (calculated) brown line corresponds to a ratio 1 between SBMIM$^{\pm}$ and TFSI^{-}. The green area points towards the best parameters σ and [SBMIM$^{\pm}$] to obtain the most repulsive samples with well dispersed NPs.

S3 Thermal Stabilities

S3.1 Coupled SANS and DLS measurements

DLS and SANS measurements were coupled at temperatures up to 473 K (200 °C). Figure S2 shows the setup of the experiments performed at PAXY, LLB. A furnace was fixed on a controlled rotating table to ensure a reproducible position for all samples. The oven was filled with nitrogen gas to work under inert atmosphere. A self-designed support for a DLS laser remote source (from Cordouan Vascoflex or VascoKin) was fixed on the rotating table, Figure S2d. Figure S2e shows the DLS remote laser source fixed on the support after turning the table by 45 ° and with a laser protection for security. As DLS measurements are fast (around 2 min for ionic liquid-based colloids analysed here) the samples were analysed during temperature changes to monitor temperature variations inside the sample. After obtaining a constant temperature, i.e., a constant DLS signal, the DLS remote laser was removed. The table was turned back to the initial position and the SANS measurement was performed. These steps were repeated at 27 °C, 70 °C, 135 °C, 200 °C and back to 27 °C. As only classical circular quartz/spacer/quartz sandwich (see Figure S2a) could fit in this furnace and no change of the furnace was possible, adapted cells were developed, making it possible to heat liquid samples in the furnace. The cells are based on a Teflon spacer glued on quartz with a hole on the top to evacuate gases that may escape during the heating process. Figure S2b shows a filled cell and in c) the cell was placed in the oven.

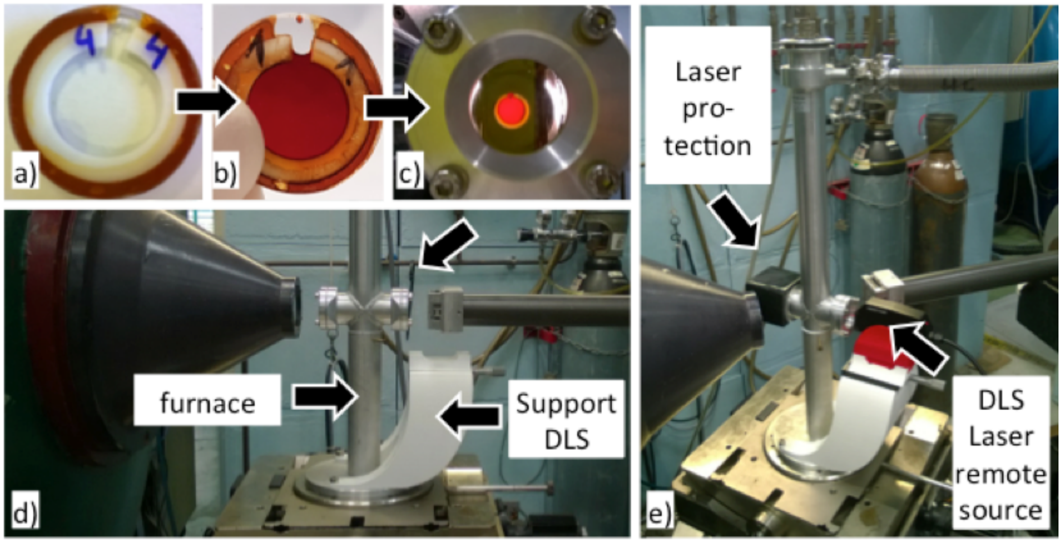

Figure S2. Scheme of the coupled SANS and DLS measurement setup at the PAXY spectrometer. a) Circular quartz/spacer/quartz sandwich with a hole on the top to evacuate gases that may form during the heating process at elevated temperatures. In b) this cell is filled with a sample and in c) it is in the furnace. d) Shows the configuration for SANS measurements and e) for DLS measurements.

Leaks occurred with concentrated samples at high temperature as mentionned in the main text. Such a leak already appeared with dilute samples ($\Phi_{NP} \approx 1$ vol%) during the tests of the cell and was solved by adapting the nature of the ring spacer (and the nature of the materials). It appeared as a mixture of wetting phenomena and bubbling/degasing at high temperature, which was not occurring in the same way depending on the nature of the materials used to build the cell. This result shows however that these wetting phenomena and bubbling/degasing grow with Φ_{NP}.
Three neutron runs were performed during which three configurations were used that slightly differed:
1st run) neutron wavelength λ=6 Å, sample to detector distance d=1m; λ=6 Å, d=3 m and λ=8.5 Å, d=5 m
2nd run) λ=5 Å, d=1m; λ=5 Å, d=3 m and λ=8.5 Å, d=5 m
3rd run) λ=4 Å, d=1m; λ=5 Å, d=3 m and λ=8.5 Å, d=5 m

DLS enables checking that equilibrium is reached before measuring SANS. This is possible as the viscosity drastically varies with temperature which influences the correlation function. Hence, stability of the correlation function means that the viscosity and temperature are stable. DLS performed after SANS tells us whether some change occurred during the SANS measurement. In addition, agglomeration not visible by eye or large viscosity changes due to a chemical evolution also invisible by eye could be detected if curves drift to longer/shorter correlation lengths (and hence time) could be saved by skipping some SANS measurements. Figure S3 shows an example for nanoparticle dispersions with SBMIM$^{\pm}$ TFSI^{-} interfacial species in EMIM TFSI. The change of the correlation functions $G_1(t)$ is driven by viscosity, leading to a shift of the correlation function without distortion. Moreover, the two correlation functions before and after heating to 200 °C superimpose (ignoring a measurement problem due to vibrations leading to oscillations in the signal).

SANS provides information on the interparticle interactions, shown here as $S(Q \rightarrow 0)$ as a function of temperature in Figure S4.

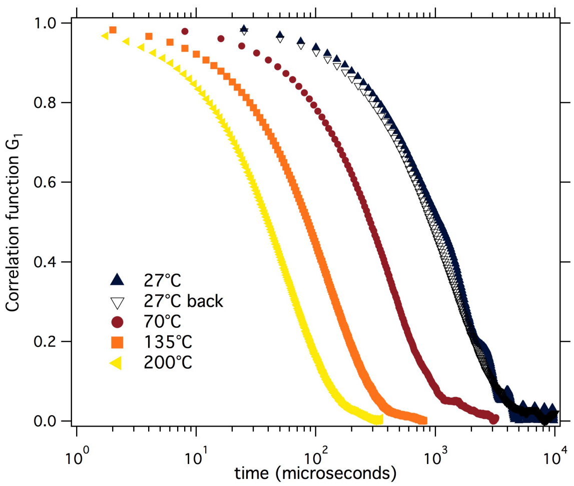

Figure S3. Dynamic light scattering (DLS) measurements for nanoparticle dispersions with [SBMIM$^{\pm}$]=0.075 mol/L in EMIM TFSI. Note that the shift of the curves is due to a change of viscosity because of the variation of temperature.

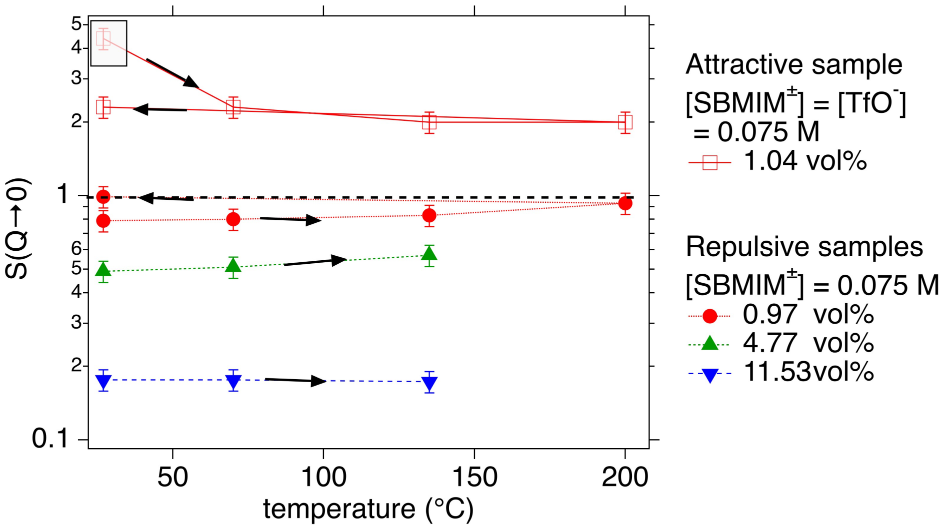

Figure S4. S(Q→0) from SANS shown in Figure 5 of the main text as a function of temperature for the attracive and the repulsive samples. The lines are guide to the eye. The arrows indicate the heating cycle. Missing points are due to leakages as explained in the text. The grey box points to an experimental artefact, not observed with SAXS, and attributed to some pollution reversibly removed while heating

S3.2 Thermogravimetric analysis (TGA)

Figure S5 presents the raw ramped thermogravimetric analysis (TGA) corresponding to the data plotted in Figure 8 of the main text. It is used to determine T_{start}, temperature at which the sample starts to loose weight, here defined for a derivative mass loss of 10 %/1 h for a heating rate of 10 °C/min (thus 1.67×10^{-2} %/ °C).
The results are summarized in Table S1 and compared with the data found in literature when possible for comparison.

Influence of the crucible: The influence of the nature of the crucible material has been tested in three samples (see Figure S6). If only a small shift is observed, between measurements in alumina and Pt crucibles, for a zwitterion SBMIM$^{\pm}$ and the repulsive dispersion at 0.97 vol%, on the contrary a strong distortion is observed with HSBMIM TFSI. As mentioned in the main text, HSMIM TFSI measured in classical Pt crucibles already decomposes at 30 °C. This can be due to a catalysis due to Pt [1] Note that alumina crucibles are better than Pt for HSBMIM TFSI, however ILs anyway tend to escape from the crucibles. As these alumina crucibles have to be set in the Pt pans due to the conception of the device, a contact between the samples and

---

[1] This has been observed for example in some ILs measured in aluminum, a material widely used for disposable pans[5].

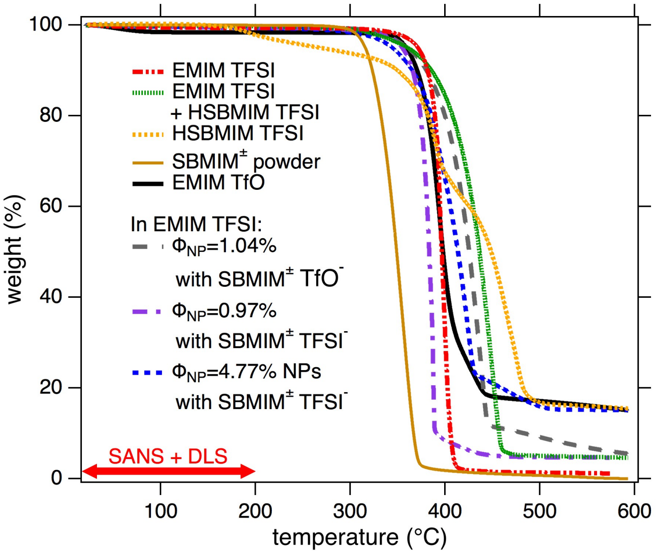

Figure S5. Ramped thermogravimetric analysis (TGA) measurements for the components of the nanoparticle dispersions in EMIM TFSI and for the resulting dispersions in EMIM TFSI. Pure EMIM TFSI and EMIM TfO are wet to mimic the worst case possible in the dispersions. Dry SBMIM$^{\pm}$ and dry EMIM TFSI containing 2.5 wt% HSBMIM TFSI are also depicted, 2.5 wt% HSBMIM TFSI being the amount added while preparing the nanoparticle dispersions at 1 vol% nanoparticles. The final dispersions with Φ_{NP}=1.04 vol% with [SBMIM$^{\pm}$]=[TfO^{-}]=0.075 mol/L as well as Φ_{NP}=0.97 vol% and a concentrated sample with Φ_{NP}=4.77 vol% nanoparticles with [SBMIM$^{\pm}$]=0.075 mol/L are also plotted. Note that all measurements are here performed in Pt pans except HSBMIM TFSI, which is decomposed close to room temperature in a Pt pan (see Figure S6). The latter is measured in an alumina crucible. The corresponding derivatives used to define T$_{start}$ are plotted in Figure 8 of the main text. The red arrow indicates the regions where SANS and DLS are performed.

the Pt can never be completely excluded. Therefore the data are compared in the Pt crucibles, except HSBMIM TFSI which is presented in an alumina crucible (in Figure 8 of the main text).

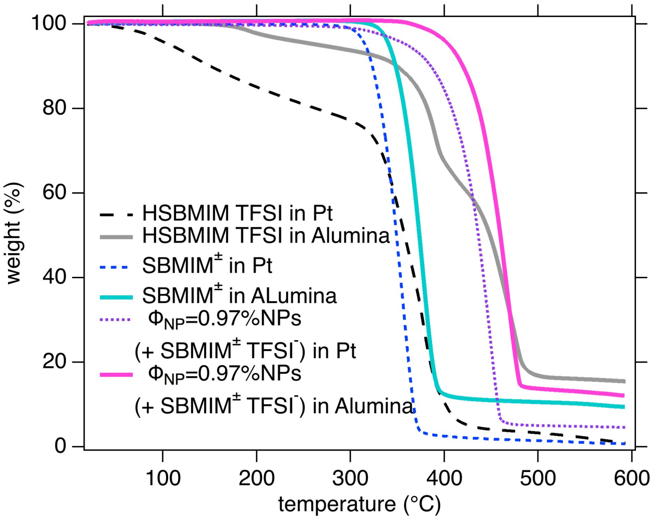

Figure S6. Ramped thermogravimetric analysis (TGA) measurements for 3 samples (see legend) either in a Pt pan or in an alumina crucible. Note that the alumina crucible has a cover, contrary to the Pt pan, which can limit evaporation if it occurs. However, this alumina crucible has still to be placed in the Pt pan and HSBMIM tends to escape from the crucible despite the cover.

Table S1. Critical temperatures (T_{start} and T_{onset}) in Celsius degrees deduced from ramped thermogravimetric analysis (TGA) measurements. T_{start} gives the temperature at which the sample starts to loose weight, here defined for a derivative weight loss of 1.67×10^{-2} %/ °C. T_{onset} is defined by the linear extrapolation of the weight loss at decomposition to the baseline at zero weight loss. All temperatures are given in °C and the error is ±10 °C* due to evaporation are removed; [i] for ionic liquid containing water.

	measured			literature			
	T_{start}	T_{onset}	weight loss after 10 h at 200 °C	T_{start}	T_{onset}	$T_{0.01/10h}$ or $T_{0.02/10h}$	$Tmax_{0.01/year}$
Φ_{NP}=1.04 vol% [SBMIM$^{\pm}$]=[TfO^{-}] =0.075 mol/L	303	393		-	-		
Φ_{NP}=0.97 vol% [SBMIM$^{\pm}$]=0.075 mol/L	303	374		-	-		
Φ_{NP}=4.77 vol% [SBMIM$^{\pm}$]=0.075 mol/L	283	377		-	-		
EMIM TfO	333 [i]	373 [i]	<0.1 %		348[1]		185[1] *
EMIM TFSI	322 [i]	386 [i]	<0.1 %[2]	320[3]	410-450[3–5]	222[3] or 252[2]	286[1] *
EMIM TFSI + 2.5 wt% HSBMIM TFSI	295	401		-	-		
SBMIM$^{\pm}$	274	325					
HSBMIM TFSI	158	305					
HSBMIM HSO_4					327[6]		
HSPMIM TfO					288[7]		

Evaporation of the samples: although seldom considered, evaporation cannot always be neglected, even for ILs. Let us consider the case of EMIM TFSI. At 200 °C, its vapour pressure is 0.02 Pa (from ref[1]), however a high amount of gas passes in TGA. In 10 hour isothermal measurement, 24 L of gas pass on 13 micro litres (around 20 mg) of sample, thus 8×10^5 $m^3_{gas} m^{-3}_{ionicliquid} h^{-1}$. If the gas saturated immediately (which is far from being the case) this would lead to complete evaporation of EMIM TFSI in around 1 minute which explains why evaporation can be observed in some ionic liquids if the carrier gas absorbs at least a bit. Note that for EMIM TFO, the vapour pressure is 0.002 Pa, 10 times lower. It means that the degradation can be overestimated from TGA measurements.

Isothermal TGA measurements are shown in Figure S7. For EMIM TFO, after a first heating to 160 °C at 20 °C/min, the weight loss is measured during three hours at 160 °C, followed by three hours at 180 °C and then ten hours at 200 °C. The weight loss is lower than 0.1 %, showing that it is long-term stable at these temperatures, here on 16 hours. A Pt pan was used.

For EMIM TFSI and the ferrofluids, the samples were heated at 20 °C/min to 200 °C before measuring the weight at 200 °C during 15h. It was done in a Pt pan and in an alumina crucible. For the pure EMIM TFSI, the container has a weak influence, as opposed to the colloidal dispersions. This is attributed to the evolution of the additive HSBMIM in Pt pans shown in Figure S6. Therefore the more exact and relevant measurements for our colloidal dispersions are the one performed in the alumina crucibles.

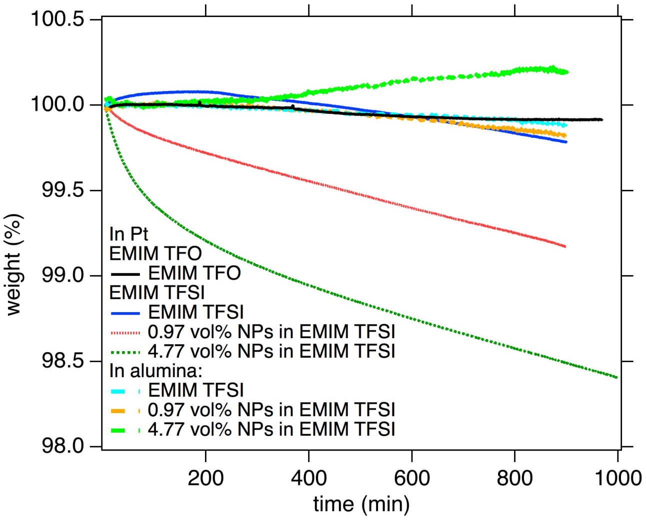

Figure S7. Isothermal thermogravimetric analysis (TGA) measurements for EMIM TfO, EMIM TFSI and the derived colloidal dispersions in two different containers. See legend and text for details.

References

1. Heym, F., Etzold, B. J. M., Kern, C. & Jess, A. Analysis of evaporation and thermal decomposition of ionic liquids by thermogravimetrical analysis at ambient pressure and high vacuum. *Green Chem.* **13**, 1453, DOI: 10.1039/c0gc00876a (2011).
2. Villanueva, M., Coronas, A., García, J. & Salgado, J. Thermal Stability of Ionic Liquids for Their Application as New Absorbents. *Ind. Eng. Chem. Res.* **52**, 15718–15727, DOI: 10.1021/ie401656e (2013).
3. Cao, Y. & Mu, T. Comprehensive Investigation on the Thermal Stability of 66 Ionic Liquids by Thermogravimetric Analysis. *Ind. Eng. Chem. Res.* **53**, 8651–8664, DOI: 10.1021/ie5009597 (2014).
4. Awad, W. H. *et al.* Thermal degradation studies of alkyl-imidazolium salts and their application in nanocomposites. *Thermochimica Acta* **409**, 3–11, DOI: 10.1016/S0040-6031(03)00334-4 (2004).
5. Ngo, H. L., LeCompte, K., Hargens, L. & McEwen, A. B. Thermal properties of imidazolium ionic liquids. *Thermochimica Acta* **357-358**, 97–102, DOI: 10.1016/S0040-6031(00)00373-7 (2000).
6. Gui, J. *et al.* Selective alkylation of phenol with tert-butyl alcohol catalyzed by Brönsted acidic imidazolium salts. *Journal Molecular Catalysis A: Chemical* **225**, 27–31, DOI: 10.1016/j.molcata.2004.08.026 (2005).
7. Amarasekara, A. S. & Owereh, O. S. Thermal properties of sulfonic acid group functionalized Brönsted acidic ionic liquids. *J Therm Anal Calorim* **103**, 1027–1030, DOI: 10.1007/s10973-010-1101-5 (2011).